Journal of The Electrochemical Society

The Role of Tungsten on the Phase Transformation Kinetics and its Correlation with the Localized Corrosion Resistance of 25Cr Super Duplex Stainless Steels

Journal of The Electrochemical Society, 2020 **167** 081510
1945-7111/2020/167(8)/081510/17/$40.00 © 2020 The Electrochemical Society ("ECS"). Published on behalf of ECS by IOP Publishing Limited

The Role of Tungsten on the Phase Transformation Kinetics and its Correlation with the Localized Corrosion Resistance of 25Cr Super Duplex Stainless Steels

Cristian Torres,[1,z] María Sofía Hazarabedian,[2] Zakaria Quadir,[3] Roy Johnsen,[1] and Mariano Iannuzzi[1,2,*]

[1]*Department of Mechanical and Industrial Engineering, Norwegian University of Science and Technology, 7491 Trondheim, Norway*
[2]*Curtin Corrosion Centre, Curtin University, Perth, WA 6845, Australia*
[3]*John de Laeter Centre, Curtin University, Perth, WA 6845, Australia*

Super Duplex Stainless Steels (SDSS) have excellent corrosion resistance due to their high concentration of alloying elements like Cr, Mo, and N. There is still, however, disagreement on the role of tungsten in the corrosion resistance of stainless steels. In this regard, the influence of tungsten on tertiary phase precipitation kinetics remains a chief source of controversy. In this study, three different SDSS with different tungsten contents have been investigated, namely, UNS S32750 (W-free), S32760 (0.6 wt% W), and S39274 (2.1 wt% W). Different isothermal aging conditions were studied, followed by microstructure characterization using scanning electron microscopy, energy dispersive X-ray spectroscopy, electron backscatter diffraction, and transmission electron microscopy to quantify the type and volume fraction of tertiary phases and intermetallic compounds. Time-Temperature-Transformation-Corrosion maps were constructed by quantifying the changes in pitting corrosion resistance caused by the precipitation of incremental amounts of deleterious phases. Results showed that 2.1 wt% W additions retarded the precipitation kinetics of all tertiary phases—including σ-phase—favoring the formation of χ-phase. Both χ- and σ-phase affected corrosion resistance, reducing the critical pitting temperature by 10 °C–20 °C at concentrations well below 1 vol%.

[DOI: 10.1149/1945-7111/ab90af]

Manuscript submitted March 30, 2020; revised manuscript received May 4, 2020. Published May 15, 2020.

It is well established that the localized corrosion resistance of stainless steels can be improved by alloying with Cr, Mo, and N.[1–4] Lorenz and Medawar[5] and later Truman[6] proposed an empirically derived parameter referred to as Pitting Resistance Equivalent (PRE) to correlate the observed localized corrosion resistance of stainless steels with composition (Eq. 1). In Eq. 1, the sub-index N indicates that the original PRE formula proposed by Lorenz and Medawar was modified to include N.[7]

$$PRE_N = \%Cr + 3.3\%Mo + 16\%N \quad [1]$$

In practical terms, the higher the PRE, the higher the resistance to localized corrosion (pitting and crevice) of the material. However, PRE and similar expressions only consider that alloying elements are in solid solution and ignore the effects of deleterious phases such as chromium carbides and σ-phase, which can precipitate during welding or improper thermomechanical processing.[7–9]

Stainless steels with higher contents of Cr, Mo, and N are required as the corrosivity of the environment increases.[10] Super duplex stainless steels (SDSS) are defined as highly-alloyed stainless steels with a PRE $\geqslant$ 40.[4,11] Currently, according to ISO 21457 and NORSOK M-001, only stainless steels with a PRE $\geqslant$ 40 can be used in natural and chlorinated seawater service.[12,13] Consequently, SDSS are widely used in the Oil and Gas offshore industry[10,14] and in other aggressive environments due to their excellent corrosion resistance and mechanical properties, the latter a consequence of their fine-grained microstructure.[15–17]

Besides Cr, Mo, and N, there are other alloying elements that improve the localized corrosion resistance of stainless steels.[18,19] It has been suggested that tungsten (W) has the same beneficial effect on passivity as Mo.[20–23] Interestingly, W is included in the PRE expression (Eq. 2) in ISO 21457.[12] In Eq. 2, the sub-index W indicates that W was also added to the original PRE expression.

$$PRE_{N,W} = \%Cr + 3.3(\%Mo + 0.5\%W) + 16\%N \quad [2]$$

However, despite the demonstrated beneficial effects on nickel alloys,[24,25] the role of W on improving the localized corrosion resistance of stainless steels remain controversial.

Effects of tungsten in solid solution.—There are several studies on the effects of W on the localized corrosion resistance of austenitic,[21,23,26–28] ferritic,[29,30] amorphous,[22] duplex,[21,31–34] super duplex[19,35–44] and hyper duplex[45] stainless steels. Although most of these investigations concluded that W improves the corrosion resistance of stainless steels, the mechanisms are still uncertain. Findings showed that, even though pure W does not form a passive layer,[26] the passive film in Fe–Cr stainless steels is improved when W is added as an alloying element.[20,27,30,46] However, this effect is less pronounced than those of Mo, when added to the same stainless steel.[20,30,46]

Researchers found that when Mo is partly substituted by W (i.e., Cr + Mo + W), the corrosion resistance of certain stainless steels further increases, demonstrating a synergetic effect between Cr, Mo, and W.[20,21,28] Additionally, according to published data,[19,31–33,37,38,47] it seems that the maximum beneficial influence of W is achieved when added at about 2–4 wt%; becoming less effective as this quantity decreases or increases and, eventually, becoming detrimental. The influence of W is more noticeable in thermally aged than in solution annealed materials, indicating a strong link between tertiary phase and intermetallic compound (IMC) precipitation kinetics and corrosion resistance.

Effects of tungsten on the precipitation kinetics of deleterious phases.—Highly alloyed stainless steels, such as SDSS, are prone to the precipitation of secondary phases (tertiary phases in the case of (S)DSS as they are dual phase materials) including IMCs, carbides, and nitrides, given their high Cr and Mo content.[4,31,35,48] The most studied deleterious phases in stainless steels are sigma-phase (σ),[1,4,29,32–39,41–45,48–60] chi-phase (χ),[4,29,32,33,36–39,41–43,45] and chromium nitrides (usually as Cr_2N).[4,49,50,58,61–63] As shown in Table I, σ- and χ-phase are rich in Cr, Mo, and W. Several studies have confirmed that σ-phase has the largest Cr enrichment, whereas χ-phase is the richest in Mo and W.[33,36,38,42,43,45,57]

Regarding the effect of W on the precipitation kinetics of deleterious phases, published works suggest that χ-phase is the

*Electrochemical Society Member.
[z]E-mail: cristian.torres@ntnu.no

Table I. Summary of the most relevant deleterious phases in DSS and SDSS.[2,5,29,32–39,41–45,48–69]

Deleterious phase	Nominal chemical formula	Crystal structure	Temperature range (°C)
Sigma (σ)	Fe–Cr–Mo (W, Mn, Si)	BCT	600–1000
Chi (χ)	Fe–Cr–Mo (W)	BCC	750–850
Nitrides	Cr_2N (CrN, less common)	HCP	700–900

primary secondary phase precipitating in W-rich stainless steels, while σ-phase is predominant in W-free SDSS.[32,37–39,41,42] Furthermore, W shifts the Time-Temperature-Transformation (TTT) curves of all deleterious phases to higher temperatures.[4,34] There is, however, a strong disagreement on the effect of W on σ-precipitation kinetics and the ability of W to reduce the total density of intermetallic precipitates.

Nilsson et al. and Hertzman et al.[36,41] concluded that W additions to stainless steels increased the density of intermetallic phases, both σ- and χ-phase. Wessman et al.[40,64] endorsed these results by means of computational simulations. These findings contrast with Kim and Kwon, Ogawa et al. and others[29,32,33,38,42,43,45] who experimentally showed that W retarded σ-phase precipitation by stabilizing χ-phase, which was later also verified by computational simulations.[34,35]

The main difference in the experimental methods between both positions lies in the heat treatment procedure. In this regard, Nilsson and Hertzman[36,41] investigated a W-free SDSS that was welded with fillers containing varying amounts of W. The samples were isothermally aged after welding. In contrast, Kim, Ogawa and others[29,32,33,38,42,43,45] isothermally treated alloys that contained W as a solid solution element.

An analysis of the results presented by Nilsson et al. and Hertzman et al.[36,41] shows that the deleterious phases nucleated faster in the W-free filler as the isothermal aging time increased in the 800 °C to 950 °C temperature range, surpassing the volume fraction of the W-rich filler at longer times. For example, at 900 °C and 1.5 min of isothermal aging, the W-free filler presented a higher density of precipitates than the W-rich filler. Therefore, it is plausible that χ-phase (mentioned by Nilsson[36] for the case treated at 900 °C and 0.5 min) was present in the W-rich filler at shorter times, delaying σ-phase formation and, thereby, reducing the total density of precipitates at longer aging times. Additionally, Wessman et al.,[40] who computationally verified that W increased tertiary phase precipitation, only considered in the simulations the growth of the intermetallic phases, not their nucleation. Consequently, it is plausible that W does play a role in the nucleation stage, but not during growth.

In contrast, Ogawa et al.[32] simulated the heat affected zone (HAZ) by controlling the heating and cooling rates of a thermal cycle performed on the samples, followed by isothermal aging. Kim and others[29,38,45] isothermally aged the samples, but they used very long aging times (up to 10 h[38]) that are not representative of the typical times involved in, e.g., welding of SDSS.[65] In addition, Park et al.[29] studied a ferritic stainless steel, Jeon et al.[45] tested a hyper duplex stainless steel (HDSS), Ahn et al.[33] focused on lab-prepared DSSs (22Cr) and Ogawa, Lee and Kim et al.[32,38,42] tested lab-prepared SDSSs. Only Akisanya et al.[43] investigated a commercial SDSS.

Correlation between the precipitation of deleterious phases and localized corrosion.—Most of the studies cited above focused separately either on the metallographic characterization of the materials[32–34,36,38,43,44] or on their corrosion properties.[19,21–23,26–28,30] Only a few investigations have linked the corrosion properties to the microstructural characterization.[29,31,37,39,41,45]

Because the precipitation of deleterious phases such as σ -phase is a diffusion-assisted transformation, a Cr-, Mo- and W-depleted zone forms around these precipitates.[4] Depleted zones have a lower localized corrosion resistance than the matrix and the precipitates, facilitating the initiation of localized corrosion in the material.[29,38,39,52–54] Among the IMCs precipitating in stainless steels, σ-phase is considered the most deleterious since it is the richest in Cr and leads to Cr and Mo depleted zones.[39]

Most studies on the effect of IMCs focused on their influence on mechanical properties rather than corrosion. It has been reported, for example, that the impact toughness of (S)DSS starts to decline when the volume of σ-phase exceeds 5–10 vol%.[4,33,43,49,66,67] In contrast, even though all studies agree on that the presence of σ-phase reduces corrosion resistance, very few investigations have reported a critical volume fraction of σ-phase responsible for the decrease in corrosion resistance of (S)DSS. Caluscio dos Santos et al.[54] found a drop in the pitting potential (E_{Pit}) of a 22Cr DSS (UNS S31803) when the volume of σ-phase was higher than 15 vol%. On the other hand, Mathiesen et al.[68] reported that corrosion resistance of DSSs (UNS S31803 and S32750), measured as changes in the critical pitting temperature (CPT), started to deteriorate when the presence of σ-phase was above 2 to 6 vol%. Deng et al.[60] observed a CPT drop of 10 °C when the σ-phase content was about 1 vol%, decreasing by more than 20 °C when the content increased above 5 vol%.

There has been, however, no systematic attempt to correlate and reconcile conflicting views on the effect of W on precipitation kinetics of SDSS and the corresponding influence in localized corrosion resistance. In this work, three SDSS with different W contents were studied, namely, UNS S32750 (W-free), S32760 (0.6 wt% W), and S39274 (2.1 wt% W). Isothermal heat treatments and advanced characterization techniques were used to investigate the role of W in the precipitation kinetics of intermetallic phases. Likewise, changes in pitting corrosion resistance were correlated with the type and volume fraction of deleterious phases. The results were combined in visual Time-Temperature-Transformation-Corrosion (TTC) maps and the implications of the findings discussed using statistical analysis.

Experimental

Materials.—Three commercial SDSS families were studied in this investigation, namely, UNS S32750, S32760, and S39274. The alloys were chosen due to their close chemical composition, except for the varying W content. As seen in Table II, UNS S32750 does not contain W, so it was used as reference material; while UNS S32760 and S39274 had 0.6 and 2.1 wt%. W, respectively. All SDSS were produced as extruded pipes with a 30 mm wall thickness and a 203.2 mm diameter.

Round samples were machined by first extracting long cylinders along the length of the pipe. The thickness of the coin-shaped

Table II. Chemical composition in wt%.

Material (UNS)	PRE_N/$PRE_{N,W}$	C	Si	Mn	Cu	Ni	Cr	Mo	N	W	Fe
S32750	43/43	0.03	0.27	0.51	0.14	6.42	25.6	3.83	0.295	—	62.9
S32760	41/42	0.03	0.50	0.60	0.60	7.1	25.2	3.6	0.254	0.62	61.5
S39274	40/43	0.02	0.24	0.71	0.52	6.3	24.9	3.1	0.29	2.1	61.8

Table III. Isothermal heat treatment temperature-time (T_xt_y) combinations.

Temperature (°C)	Time (s)
T1 = 790	t1 = 60
	t2 = 120
	t3 = 240
	t4 = 600
	t5 = 1200
T2 = 846	t1 = 60
	t2 = 90
	t3 = 120
	t4 = 240
	t5 = 600
	[a)]t6 = 1200
T3 = 920	t1 = 60
	t2 = 120
	t3 = 240
	t4 = 600
	t5 = 1200

a) heat treatment only performed in UNS S39274 for the TEM analyses due to the low density of tertiary phases present at lower times.

specimens was 3 mm and the diameter 25 mm for UNS S32750 and S32760 and 30 mm for S39274. Unless specified otherwise, all tests were performed in duplicate.

Heat treatments.— *Solution annealing (SA).*—Even though the pipes were received in the solution annealed condition, all samples were re-solution annealed at 1100 °C for 15 min in an air furnace and rapidly quenched in water according to the recommendations of the alloy suppliers. SA was performed to remove all possible undesirable phases, and to ensure the homogeneity of the microstructure. Light optical microscopy (LOM) and electron backscatter diffraction (EBSD) measurements—performed as described below—showed that the average ferrite and austenite volume fractions were within the specified range, namely, 57–43, 60–40, and 48–52 vol%, for the UNS S32750, S32760, and S39274 SDSS, respectively.

Isothermal heat treatments (IHT).—Isothermal aging was carried out on the SA samples in an air furnace followed by quenching in water. The isothermal aging conditions were chosen based on the work by Nilsson et al.[4] Table III summarizes the selected time and temperature combinations. The highest temperature (T_3 = 920 °C) was chosen to avoid χ-phase precipitation, which is critical to examine the independent effect of σ-phase. The intermediate temperature (T_2 = 846 °C) was chosen to achieve a rapid σ-phase precipitation as reported for SDSS.[4] Lastly, a larger density of χ-phase was expected[4] at the lowest temperature (T_1 = 790 °C), which helped emphasize and separate its impact from the other precipitates. T1, T2, and T3 represent the actual temperature measured on the samples to which a K-type thermocouple was attached during each IHT.

The specimens were introduced in the furnace after reaching the set-temperature. Only two coin-shaped samples were included per IHT batch to minimize the thermal mass introduced into the furnace. Additionally, handling two specimens at the time reduced the handling time and ensured that the furnace door was open for a very short time. The temperature was recorded by attaching a thermocouple to one of the samples. The temperature drop observed immediately after introducing the specimens was under 10 °C, and it took less than 1 min for the coupons to reach the target temperature.

Changes in the austenite and ferrite volume fractions caused by IHT were also measured by LOM and EBSD as detailed below. The austenite and ferrite content remained in the accepted range for SDSS, i.e. 40–60 vol% for all materials.

Sample preparation.— *Polishing.*—After IHT, the samples were wet-ground and polished down to 1 μm diamond suspension to obtain a mirror-like surface finish. Afterwards, the samples were rinsed with acetone, followed by rinsing with distilled water and cleaned with ethanol in an ultrasonic bath for 5 min.

Etching.—Samples analyzed with LOM, scanning electron microscopy (SEM), and energy-dispersive X-ray spectroscopy (EDS) were etched following Statoil technical note MAT-2010080[69] to facilitate the identification of tertiary phases during the sample characterization stage described below. The etching procedure consisted of two steps. In the first step, a 15 wt%. KOH solution was used, and a potential of 3 V applied for 12 s. In the second step, the solution was 20 wt%. NaOH with an applied potential of 1.5 V for 10 s.

Electropolishing.—Only for those samples analyzed with EBSD, extra surface preparation steps were followed after polishing to remove the deformation structure left by abrasive polishing, which is known to affect EBSD results.[70] After the 1 μm diamond particle polishing, the samples were electropolished using a solution of 5.3 vol% H_2SO_4–94.7 vol% methanol at 18 V for 30 s; followed by a final polishing step using an oxide polishing suspension (OPS) of a 0.02 μm colloidal silica.[71,72]

Transmission electron microscopy specimens.—The various types of precipitates were further analyzed by transmission electron microscopy (TEM), high-resolution (HR) TEM, scanning transmission electron microscopy (STEM), TEM-EDS, and selected area electron diffraction (SAD). Thin foils were prepared via focused-ion beam (FIB) milling using a Tescan Lyra dual beam FEG SEM platform from the UNS S32750 and S39274 samples treated at T2 for t4 and at T2 for t6, respectively. Detailed information on the sample preparation by FIB can be consulted elsewhere.[73,74]

Sample characterization.—Different microscopy techniques were employed to characterize the microstructure of the samples after the isothermal aging, as follows.

Light optical microscopy.—An infinite focus microscope (IFM) was used with magnifications that varied between 10× and 50× to observe the overall sample microstructure, i.e., austenite (γ), ferrite (α), and the presence of deleterious phases.

Back scattered electron (BSE) imaging.—All the samples were investigated using SEM in the BSE imaging mode. BSE was chosen as it is more sensitive to variations in composition, facilitating the identification of different phases. In this regard, heavier elements (e.g., W) appear brighter while lighter elements appear darker in BSE images.[4,36,75] The electron beam was used with an acceleration voltage of 20 kV, with a 30 μm diameter aperture and a spot size of 3, resulting in a beam current of approximately 0.16 nA.

Energy dispersive X-ray spectroscopy.—Once the tertiary phases were located by BSE imaging, their chemical composition was analyzed by EDS. The electron beam was changed to an accelerated voltage of 20 kV, with a 50 μm diameter aperture and a spot size of 5, giving a beam current of approximately 7.2 nA. The point analysis tool was used to acquire the composition of only the deleterious phase and not the surrounding area. At least 10 points were taken per phase. EDS results were compared as a function of IHT temperature and time. Nevertheless, since the actual depth and area affected by the electron beam are unknown, the composition obtained by SEM-EDS was regarded as qualitative. Consequently, a definite conclusion could not be drawn by EDS alone as the variance of some of the

results was considerable, particularly for small (<1 μm) deleterious phases.

Electron backscatter diffraction.—Volume fraction calculations of the different phases were obtained from the EBSD maps. All analyses were performed at an 800× magnification to ensure an area large enough to compare between samples. The electron beam was used with an acceleration voltage of 20 kV, with a 50 μm diameter aperture and a spot size of 5, resulting in a beam current of approximately 7.2 nA. The acquisition settings consisted of a frame rate of 40 fps, a resolution of 256 × 256 px and an exposure time of 24500 μs. The confidence index (CI) obtained was always higher than 0.1.

Transmission electron microscopy.—Bright-field (BF), high-resolution (HR) TEM and STEM were conducted using a FEI Talos FS200X G2 field emission gun (FEG) TEM operating with an electron beam at 200 kV acceleration voltage. Samples were tilted to a prominent zone axis with a double tilt holder and the selected area the diffraction pattern was obtained with a high-resolution camera. The SAD patterns were obtained using a 200 nm diameter aperture for selecting the area of interest, indexed manually and compared to the literature to confirm the crystal structure of the phases identified by EBSD. Additionally, the chemical composition of the precipitates was obtained in STEM mode using EDS mapping. EDS was conducted using two pairs of FEI Super X detectors. The EDS and STEM data were acquired and analyzed with Velox software.

Corrosion testing—critical pitting temperature.—Once the tertiary phases were identified and quantified for each sample, corrosion tests were carried out to evaluate the impact of the deleterious phases on the pitting corrosion resistance of the materials. Isothermally aged specimens were freely exposed in a 6 wt% $FeCl_3$ environment (pH = 1.2) while the temperature was increased in steps.[19,76] The surface exposed to the electrolyte (12.1 cm^2 for UNS S32750 and S32760, and 16.9 cm^2 for UNS S39274) was polished down to a 1 μm diamond suspension as explained above. The specimens were suspended using a 200 μm Pt wire to avoid crevice corrosion.[19] A small hole, approximately 2 mm in diameter, was drilled on the sample to pass the Pt wire. Then, the full sample was immersed in the electrolyte. If signs of crevice corrosion were found after testing, the sample was discarded, and the experiment repeated.

The tests started at 40 °C and the temperature was increased 5 °C every 24 h until observing localized corrosion. Between steps, the temperature was increased as quickly as possible. The temperature was controlled using a hot plate and kept within ±1 °C at each step. The open circuit potential (OCP) was monitored during exposure and used as an indication of pitting corrosion initiation, as explained elsewhere.[19,77] Mathiesen et al.[77] reported localized attacks on SDSS samples once the OCP decreased below +500 mV vs standard calomel electrode (SCE). Hence, this value was arbitrarily chosen as the threshold to define the CPT.

After exposure, samples were analyzed with IFM and SEM to document the location of the localized corrosion attacks. All corrosion tests were conducted in duplicate to verify reproducibility.

Statistical analysis.—Given the large number of conditions, statistical analysis was performed to evaluate whether the influence of the heat treatments and alloy composition on CPT values was significant. The statistical analysis considered two factors: (i) the type of material (i.e., UNS S32750, S32760, and S39274) and (ii) the isothermal heat treatment condition (i.e., the 15 different temperature-time combinations shown in Table III). Since each corrosion test was carried out in duplicate, a two-way ANOVA with replication[78,79] was chosen as the statistical tool to determine if there were significant differences between the three materials, the different heat treatments, or both with a 95% confidence (i.e., a p-value lower than 0.05).

Unfortunately, the ANOVA test cannot be used to determine the specific materials or heat treatments that result in the statistically significant differences in CPT. Hence, further analyses using the so-called Post-Hoc tests were required. Post-Hoc tests perform pairwise comparisons between different groups of the factors studied in the ANOVA. The goal of the Post-Hoc tests is to identify the group(s) that lead to a significant difference. A type I error, i.e., concluding that there is a significant difference when there is none, is a common issue that might appear when performing multiple comparisons using the same dataset. This is because a type I error (5% for p-values equal to 0.05) gets added for each comparison performed in the same dataset. Consequently, if enough comparisons are carried out, the type I error could reach 100% and, hence, cause a wrong result in the Post-Hoc test. For this study and given the large number of multiple comparisons, the Bonferroni test was chosen.[80] The Bonferroni test was developed to avoid data incorrectly appearing as statistically significant (type I error).[80] The Bonferroni analysis included a correction to the p-value, which consists of dividing the p-value (i.e., the type I error) by the total number of comparisons performed to the data. Thereby, the type I error for the total number of pairwise comparisons was 5%. The Bonferroni test has been, nonetheless, criticized for being overly conservative.[81] Thus, a second Post-Hoc test referred to as Tukey test[82] was also performed and the results compared with the Bonferroni approach. In contrast to the Bonferroni method, the Tukey approach used the so-called Honestly Significant Difference (HSD) parameter. The HSD test compares the differences between "means of values" rather than comparing pairs of values. The parameter HSD is calculated from the ANOVA result as shown elsewhere.[82] Thereby, if the averages of the conditions being compared differ by more than the HSD, the difference between them is considered significant. An example of the calculation can be consulted elsewhere.[79]

Results

Phase identification and microstructure evolution.—In light optical micrographs, σ- and χ-phases appeared, in most cases, as dark spots or small blue areas at the γ/α interfaces. Figure 1 illustrates the precipitation of tertiary phases in different conditions, as indicated by the arrows. In Fig. 1, bright and dark phases correspond to austenite and ferrite, respectively.[51,54,83–85]

Figures 2 to 4 present a series of BSE images that summarize the structures of the three SDSS samples at different IHT conditions, as indicated. The γ and α phases were identified from their relative bright and dark contrasts and checked later by EBSD phase identification. Deleterious phases appeared brighter than both matrix phases, indicating an enrichment of heavy elements in their composition.[4,36,75] In this regard, BSE imaging has been proposed as a reliable method to identify χ-phase given its higher W content.[4] In all cases, the amount and size of precipitates increased with higher temperature and longer aging times. In Figs. 2 and 3 (UNS S32750 and S32760, respectively), the precipitates preferentially grew from the γ/α interface into the α grains as the IHT time increased. In contrast, in Fig. 4 (UNS S39274), the density of precipitates increased at γ/α interfaces and, ultimately, precipitation occurred inside the α grains.

As seen in Figs. 5a–5c, there were two predominant phases precipitating in all three materials. One phase was brighter and smaller, whereas the second phase was larger and duller than the other phase, but still brighter than the matrix. The latter precipitate appeared in higher quantities in UNS S32750 and S32760, whereas the former was the main phase nucleating in S39274. Both phases formed at γ/α interfaces. At longer isothermal aging times, the bright phase nucleated inside the α grains as well, whereas the duller one grew from the grain boundaries into the α grains as seen in Fig. 5d.

Table IV summarizes the average chemical composition obtained by EDS of every phase observed in the BSE for the three SDSSs. The main differences were in their Mo and W (for those materials containing W) content. All tertiary phases (σ and χ) were richer in

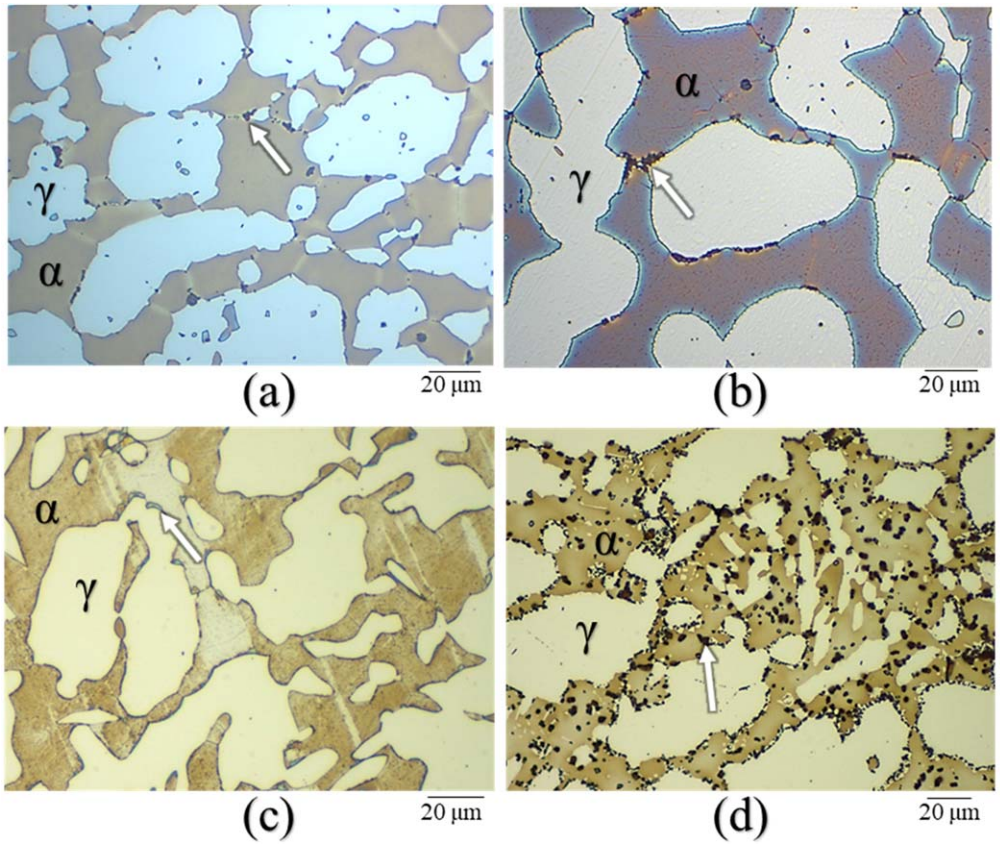

Figure 1. Light optical microscopy after isothermal aging (a) UNS S32750 at 846 °C for 240 s, (b) UNS S32760 at 920 °C for 240 s, (c) UNS S39274 at 846 °C for 600 s and (d) UNS S39274 at 920 °C for 1200 s. White arrows point at deleterious phases. Bright and dark phases correspond to austenite and ferrite, respectively.

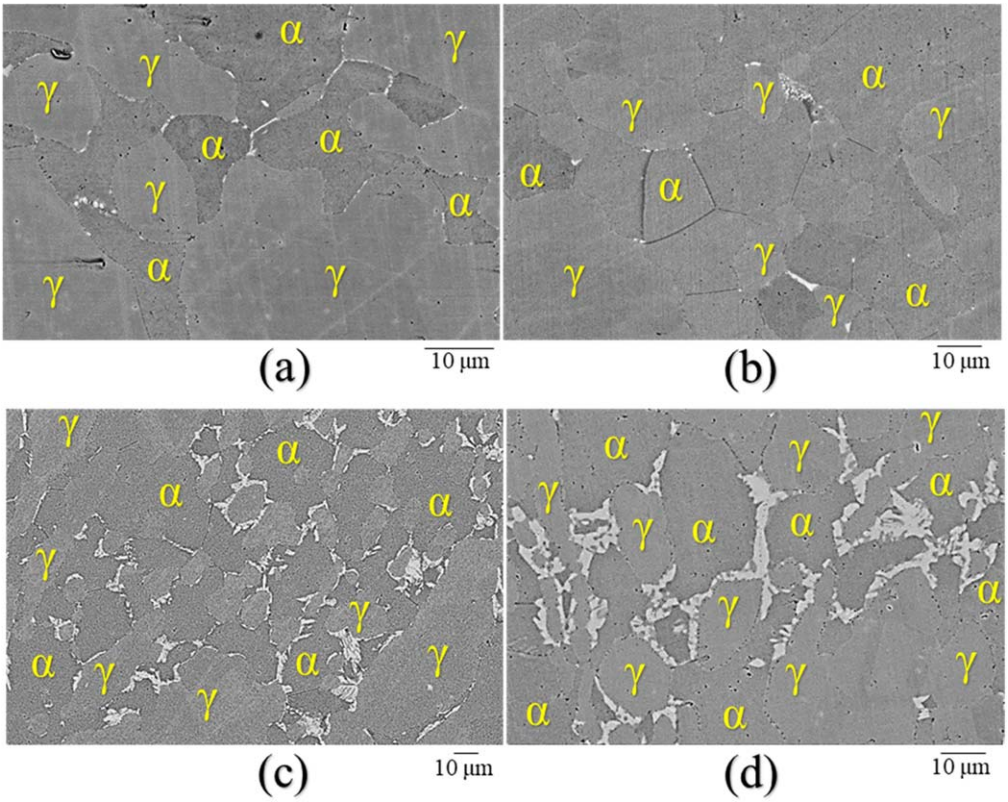

Figure 2. Scanning electron microscopy after isothermal aging of UNS S32750 at (a) 790 °C for 600 s, (b) 846 °C for 240 s, (c) 846 °C for 600 s and (d) 920 °C for 600 s.

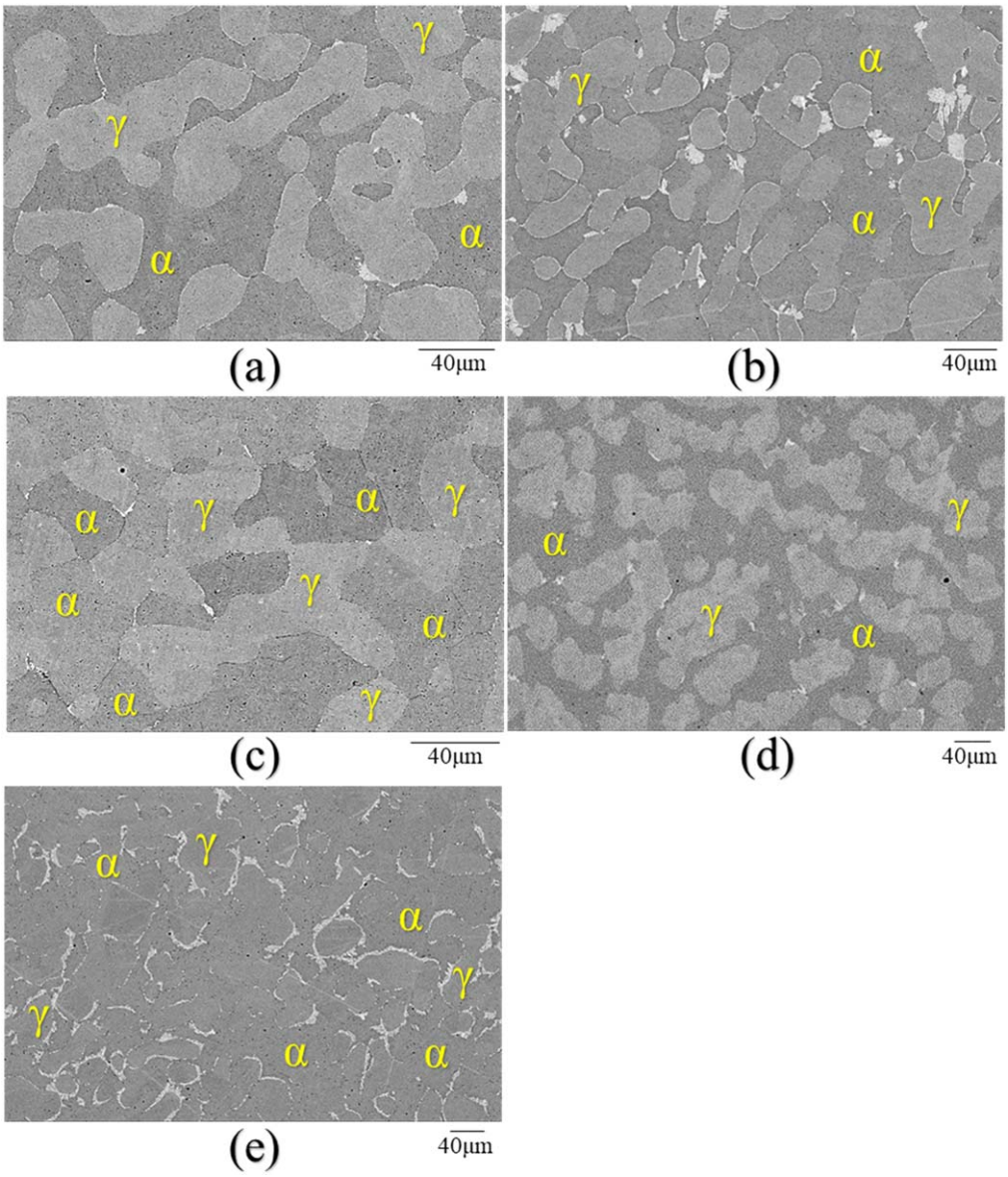

Figure 3. Scanning electron microscopy after isothermal aging of UNS S32760 at (a) 790 °C for 600 s, (b) 790 °C for 1200 s, (c) 846 °C for 240 s, (d) 920 °C for 240 s and (e) 920 °C for 600 s.

Cr, Mo, and W than the matrix (i.e., α and γ). In the case of the W-free SDSS, χ-phase was enriched only in Mo, while σ-phase had a higher Cr and Mo content than both γ and α. For the samples containing W, both tertiary phases were also enriched in W relative to the matrix. These findings confirmed that bright precipitates were χ-phase, while the other particles were σ-phase.[4,36] These results were consistent across all the samples investigated in this study.

EBSD results validated the SEM-EDS analysis. Figure 6 shows the main phases that precipitated in UNS S32760 and S39274 after isothermal aging, as indicated. σ-phase precipitated after short IHT times (i.e., 120 s) in both UNS S32750 and S32760. The size and amount of σ-phase increased with the duration of the IHT. While σ-phase was predominant in UNS S32750 and S32760, χ-phase was the main phase found in S32794. In fact, σ-phase was only detected in UNS S39274 after long (i.e., 1200 s) isothermal aging times and in very small quantities.

TEM was used to confirm EBSD results. Figures 7 to 10 show HR-TEM images, SAD patterns, and STEM-EDS data of the tertiary phases in the UNS S32750 and S39274 samples, respectively. The HR-TEM image and SAD pattern of the intergranular precipitate in the S39274 (Fig. 7) sample were consistent with the BCC χ-phase structure.[86] The corresponding chemical composition analysis of χ-phase in Fig. 8 showed a high Cr and Mo content, but no clear enrichment in W. This lack of a clear W enrichment was attributed to an experimental limitation, as EDS did reveal a clear W enrichment in larger precipitates. The higher W content leads to a brighter region in BSE SEM images. This difference in brightness was used to differentiate between χ and σ as explained by Jackson et al.[75] Furthermore, it was possible to qualitatively observe the depleted zone between both phases, i.e., a small area which was poorer in Cr and Mo adjacent to χ-phase as indicated, although no clear W gradient was found. Similarly, the SAD pattern obtained from the UNS S32750 tertiary phase (Fig. 9) was in good agreement with the tetragonal crystal structure of σ-phase.[87] The chemical analysis in Fig. 10 confirmed the Cr and Mo enrichment of the σ-phase. The formation of secondary austenite (γ_2) was verified as well by its low Cr and Mo content and the relative Ni enrichment.[55] Additionally, a nanosized phase rich in Cr and N was observed within σ-phase. Given its chemical composition, the phase was consistent with Cr_2N commonly found in SDSS.[4,48,57,61]

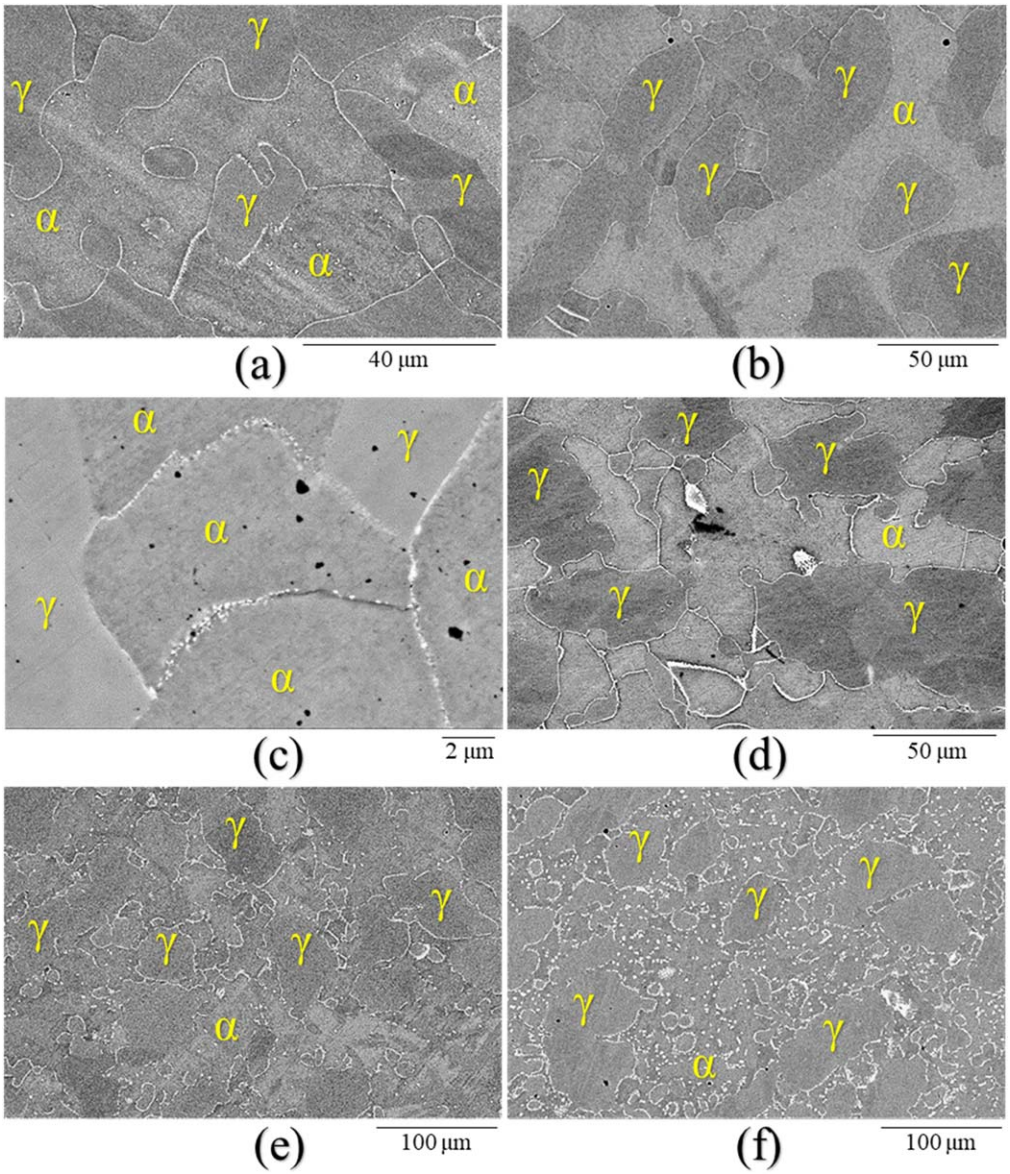

Figure 4. Scanning electron microscopy after isothermal aging of UNS S39274 at (a) 790 °C for 600 s, (b) 790 °C for 1200 s, (c) 846 °C for 240 s, (d) 846 °C for 600 s, (e) 920 °C for 600 s and (f) 920 °C for 1200 s.

Phase quantification.—Once the deleterious phases were identified, their volume fractions were measured for each IHT condition. Although EBSD analysis can provide the volume fraction of each phase directly, unfortunately, it failed to distinguish between α and χ-phase unambiguously as both have a BCC crystal structure. Thus, only the vol% of γ and σ-phase could be measured directly from the EBSD results. The α and χ-phase were quantified together as the sum of both phases. Subsequently, an open-access image processing software was used to obtain the total vol% of all deleterious phases from the BSE SEM pictures. The phase quantification was achieved by filtering the deleterious phases that appeared brighter in these BSE pictures from the background (γ and α). The χ vol% was quantified by subtracting the total vol% of deleterious phases from the σ vol% determined by EBSD. Lastly, once the amount of χ-phase was known, the α vol% could be obtained from the EBSD results. At least ten pictures of each microscopy technique were used for each IHT condition.

Corrosion testing.—Figure 11 illustrates an example of the pitting corrosion test results for the three SDSS in identical IHT conditions, whereas Fig. 12 shows the CPT values obtained for all specimens as a function of IHT time and temperature, as indicated. CPT values decreased with isothermal aging time for all samples at all temperatures, falling faster for UNS S32760, S32750, and S39274, in order. The decline in the CPT values was faster at 846 °C for all three materials. In all instances, localized corrosion started at the interface between the matrix and the different precipitates, as illustrated in Fig. 13.

Temperature–time–transformation-corrosion diagrams.—TTTC diagrams were constructed for each alloy considering the average vol% of the deleterious phases and the lowest CPT result for each condition, as illustrated in Figs. 14 to 16. Each point in the TTTC plots was drawn according to the type of microstructure observed, as follows. (i) An empty circle indicates no tertiary phase precipitation (within the resolution limits of the techniques used herein), i.e., the microstructure was similar to the SA sample; (ii) a half-full circle indicates that either (a) precipitates were found but their amount was small, and no quantitative identification was possible or (b) both types of precipitates (σ and χ) were present in small but similar quantities; (iii) a circle with a cross inside indicates that the main tertiary phase was χ-phase and, finally, (iv) a full black circle indicates that the main

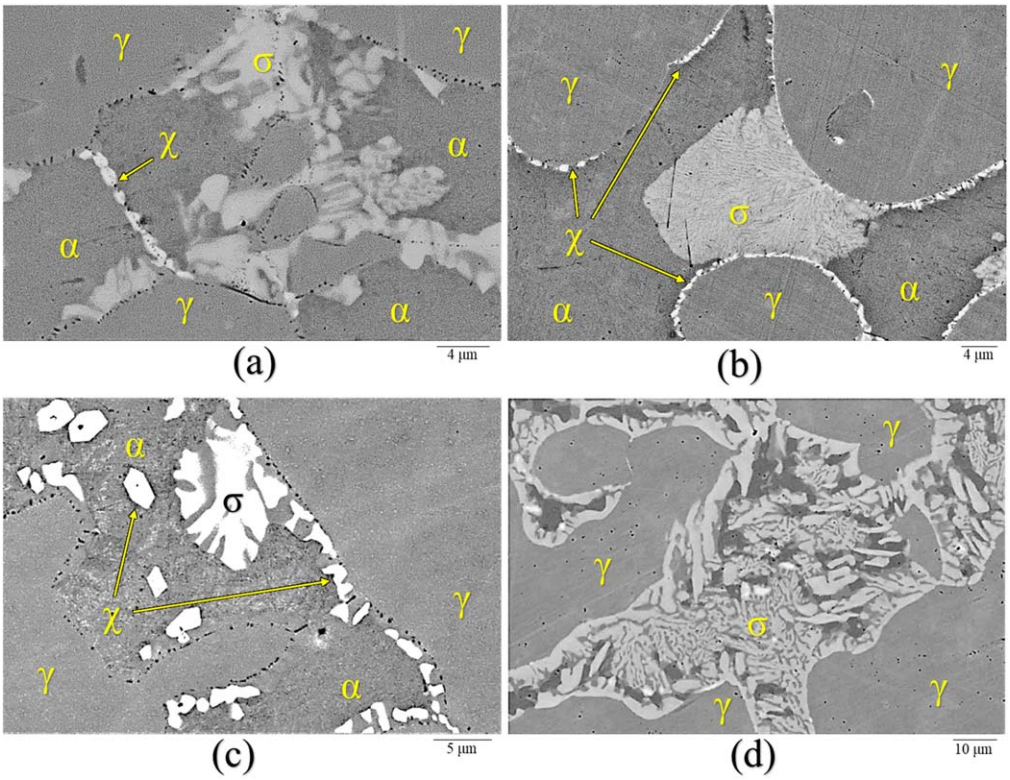

Figure 5. Scanning electron microscopy after isothermal aging of (a) UNS S32750 at 846 °C for 600 s, (b) UNS S32760 at 790 °C for 1200 s, (c) UNS S39274 at 920 °C for 1200 s and (d) UNS S32760 at 920 °C for 1200 °C.

Table IV. Average chemical composition of each phase in wt%.

Material (UNS)	Phase	Fe	Cr	Ni	Mo	W
S32750	Ferrite (α)	63.9	28.1	4.6	3.6	—
	Austenite (γ)	64.9	25.2	7.5	2.3	—
	Sigma (σ)	59.0	30.0	4.4	6.4	—
	Chi-phase (χ)	56.0	28.9	3.7	11.5	—
S32760	Ferrite (α)	62.2	27.0	5.3	3.1	0.75
	Austenite (γ)	63.3	23.9	8.3	2.1	0.6
	Sigma (σ)	57.7	29.9	4.4	5.2	1.0
	Chi-phase (χ)	53.9	27.2	4.3	10.8	2.1
S39274	Ferrite (α)	63.5	26.4	4.7	2.9	2.5
	Austenite (γ)	64.7	24.1	7.3	1.9	1.9
	Sigma (σ)	55.2	29.7	3.7	6.6	4.5
	Chi-phase (χ)	52.0	25.2	3.7	10.8	9.5

precipitate was σ-phase. The volume fraction of the phase calculated from the microscopy techniques was included below the circle, whereas the CPT value was added on top. In the case when the phases could not be successfully identified, the total volume fraction was reported together as the sum of all precipitates. In this manner, all data is gathered in the same plot, facilitating a visual and straightforward analysis.

Statistical analysis.—Table V shows the results of the ANOVA calculations. The p-value obtained for the interaction between the materials and the heat treatments was lower than 0.05, meaning that there was a statistically significant difference on the CPT values as a function of composition and heat treatment condition. Consequently, the Pot-Hoc tests were carried out to find the specific significant difference in CPT values

Both Post-Hoc tests yielded similar results for each pairwise comparison between the two factors. The first part of the tests consisted of pairwise comparisons between isothermal aging times within each material and temperature to find if a significant difference in the CPT values existed. The results are summarized in Table VI. UNS S32750 and S32760 showed that the CPT change was significantly different at the same aging times for the three different aging temperatures. On the other hand, UNS S39274 experienced a significant CPT drop at longer IHT times at 846 °C, whereas the drop occurred at the same IHT time at 790 °C. The significant drop obtained at 920 °C, although logical since it was a drop of 15 °C, cannot be compared with the other two alloys since the corresponding CPT was 60 °C, much higher than for the other two materials.

Table V. Results obtained from two-way ANOVA with replication of CPT values. (SS: sum of squares, df: degrees of freedom, MS: mean square).

Source of variation	SS	df	MS	F-ratio	P-value
Factor A: Material	1007	2	504	64.8	$5.2{\cdot}10^{-14}$
Factor B: Heat treatment	15132	14	1081	139.0	$3.5{\cdot}10^{-32}$
Interaction: Material * Heat treatment	1059	28	37.8	4.9	$1.4{\cdot}10^{-6}$
Error (within)	350	45	7.8		
Total	17549	89			

The second part of the Bonferroni and Tukey tests consisted of a pairwise comparison of each heat treatment condition between the three materials. Table VII shows the heat treatments that exhibited statistically significant differences between different materials. UNS S32750 and S32760 were only significantly different at one heat treatment (790 °C, 240 s). In contrast, S39274 was significantly different from the other two materials at two different heat treatments, namely, 846 °C, 240 s and 920 °C, 600 s.

Discussion

Precipitation kinetics.—Many publications[4,31,37,42,43,45,48,51,55–57] report that the precipitation of both σ- and χ-phase starts at the γ/α interface, similar to what has been observed in this work. The mechanism by which σ-phase precipitates has been described as an eutectoid reaction[51,55,59] (Eq. 3) where ferrite (α) splits into σ-phase and a γ_2, which has a lower Cr and Mo content than in the original γ-phase.[4,55,88] The α-stabilizing elements, such as Cr and Mo, form σ-phase, while the austenite stabilizing elements like Ni diffuse out, leading to the formation of γ_2. On the other hand, the austenite stabilizers are enriched in the γ_2, while the α stabilizers are expelled helping the growth of σ-phase.[55] This reaction gives σ a lamellar structure, which can be seen in Figs. 5a–5c. Even though the lamellar eutectoid morphology has been described only for temperatures under 900 °C[55]; in this work, lamellar eutectoid σ-phase formation occurred as well at 920 °C for UNS S39274 as shown in Fig. 5c. For the other SDSS, γ_2 developed below 900 °C, whereas above 900 °C σ-phase precipitation followed the divorced eutectoid mechanism described by Kobayashi et al.[55] and illustrated in Fig. 5d. This difference in the temperature range can be explained by the fact that W shifts the TTT curves to higher temperatures.[4,34] Therefore, it is reasonable to expect that the eutectoid σ-phase reaction occurred above 900 °C if the material contained enough W. In the case of UNS S32760, it seems that 0.6 wt% W was insufficient to affect the phase precipitation mechanism.

$$ferrite(\alpha) \rightarrow sigma(\sigma) + secondary\ austenite\ (\gamma_2) \qquad [3]$$

Another consequence of the shift of TTT curves caused by W is that the fastest precipitation kinetics takes place at higher temperatures, explaining why both W-rich materials had a higher density of intermetallic phases at 920 °C than the W-free UNS S32750. In contrast, the largest amount of precipitates was found at 846 °C for the W-free SDSS.

The main difference between the materials was, however, the effect of high-W additions (i.e., 2.1 wt%) on σ- and χ-phase precipitation. In this regard, while σ-phase was the main IMC present in UNS S32750 and S32760, χ-phase was almost the exclusive tertiary phase in S39274. Indeed, depending on the IHT condition, χ -phase precipitation inhibited or retarded the nucleation of σ-phase and decreased the total amount of deleterious phases.

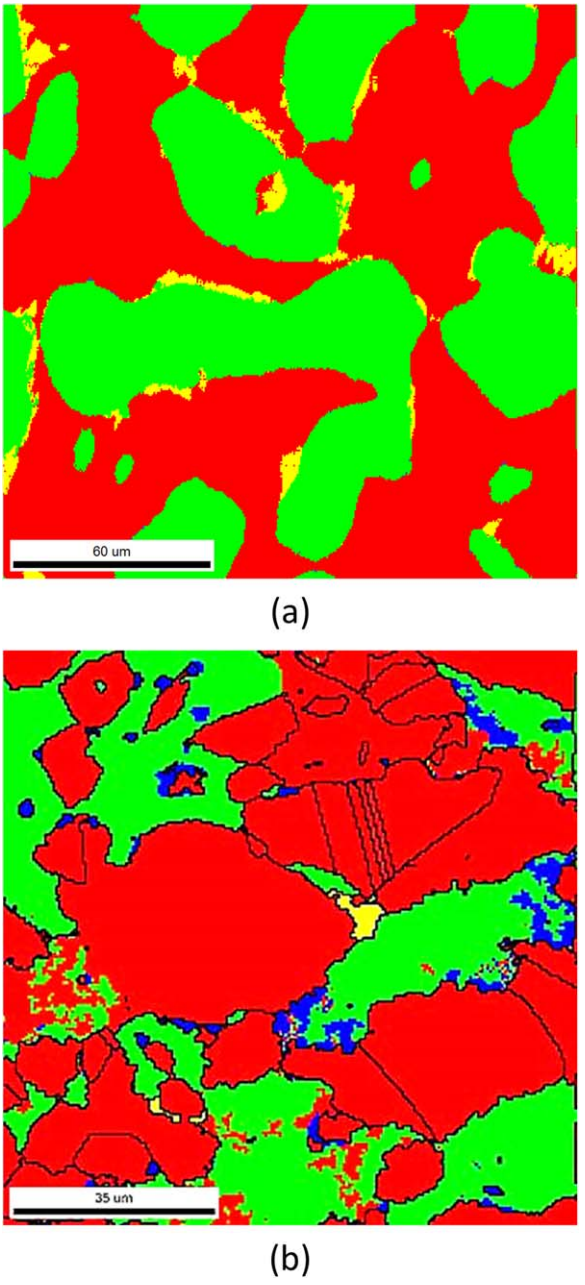

Figure 6. EBSD map of heat treated (a) UNS S32760 at 846 °C for 1200 s and (b) UNS S39274 at 920 °C for 1200 s (red = austenite, green = ferrite, blue = chi, yellow = sigma).

Table VI. Heat treatment times at which CPT was significantly different (p-value < 0.05) for each IHT temperature and material according to Bonferroni and Tukey tests.

	Heat treatment				
Material (UNS)	T (°C)	t (s)	CPT (°C)	CPT drop (°C)	Secondary phases (vol%)
S32750	790	600	<40	>30	0.2% σ, 0.1% χ
	846	240	50	20	0.3% σ
	920	600	45	25	3.1% σ, 0.1% χ
S32760	790	600	<40	>15	0.9% σ, 0.4% χ
	846	240	45	20	0.2% σ, 0.2% χ
	920	600	<40	>20	5.1% σ, 0.3% χ
S39274	790	600	50	10	0.11% χ, 0.03% σ
	846	600	<40	>15	1.4% χ, 0.3% σ
	920	240	60	15	0.6% χ

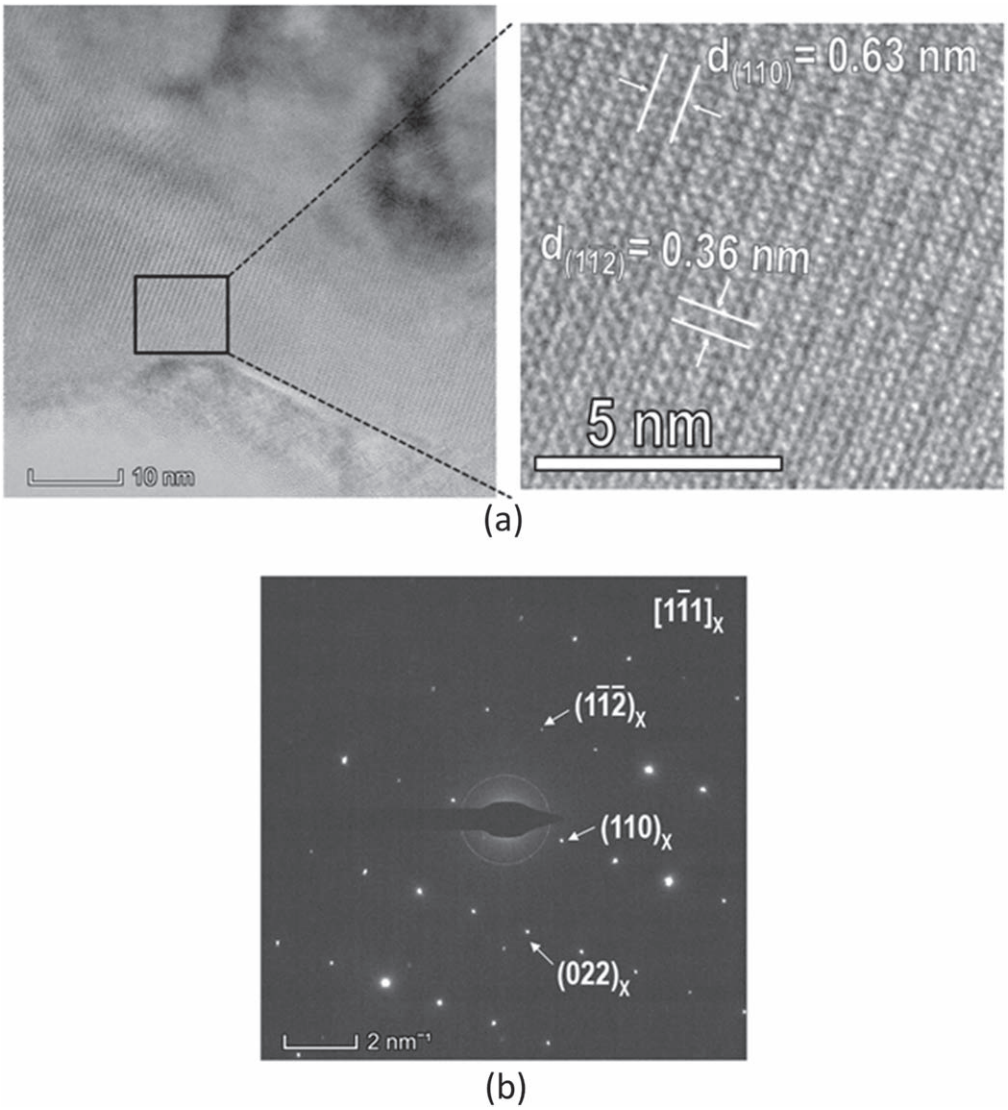

Figure 7. TEM analysis of χ-phase precipitate formed in UNS S39274 steel treated T2 for t6. (a) HR.TEM and (b) indexed SAD pattern of the χ-phase parallel to the [1$\bar{1}$1] zone axis.

Although the retardation of σ-phase precipitation kinetics by χ -phase has been attributed to the high W content, the mechanisms are unclear.[23,26,32,42,89] Some authors[32,37,39,41,42] have reported that, while stainless steels based on Fe–Cr–Mo promote σ-phase precipitation, χ-phase nucleates when Mo is partly substituted by W (Fe–Cr–Mo–W), slowing the kinetics of the σ-phase precipitation down. It has been suggested that the decomposition of α into σ (as shown in Eq. 3) is delayed given the much slower diffusion of W in ferrite than Mo.[32,42,90–93] In this regard, some researchers[42,90] have reported that Mo diffusivity in α was one order of magnitude faster than W, whereas others[32,91–93] obtained diffusivities two to three times slower for W compared to Mo. Consequently, α is stable longer when the alloy contains W and this undiffused W favors, instead, the nucleation of χ-phase.[42] Another explanation proposed by Ogawa et al. and Lee et al.[35,42] is that the interfacial energy between χ-phase and α is lower than that between σ-phase and α since χ and α both have BCC structures, while σ is tetragonal. Once χ-phase precipitates first, σ is delayed as the nucleation sites are occupied, i.e., there is not enough Cr and Mo to precipitate σ-phase.[32,38,45]

In this study, σ-phase was the predominant tertiary phase that nucleated in UNS S32760 despite its 0.6 wt%. W, suggesting that the W concentration was small to affect precipitation reactions. Results also suggested that there exists a W-content range where χ-phase becomes predominant, delaying σ-phase formation. Moreover, given that UNS S32760 exhibited the highest density of total deleterious phases in almost all the temperature-time combinations, W could become detrimental outside the suspected optimal range.

Pitting corrosion resistance.—The difference in precipitation kinetics resulted in a difference in the degree of corrosion attack. In the specimens where σ-phase was the main deleterious phase, the attack occurred in the γ_2 regions, as seen in Fig. 13b. In contrast, in samples where χ-phase was the primary precipitate, localized corrosion initiated at the χ-phase/matrix interface. Since χ-phase formed predominantly at grain boundaries, intergranular corrosion occurred on those specimens with a large vol% of χ-phase (Fig. 13c). Pitting corrosion was observed in the SA samples, which occurred predominantely in the austenite regions and in some ferrite grains, as illustrated in Fig. 13a.

CPT values decreased with isothermal aging due to the higher density of tertiary phases in the microstructure as the TTTC maps (Figs. 14 to 16) illustrate. As seen in Table VI, UNS S32750 and S32760 experienced the statistically significant CPT drop at the

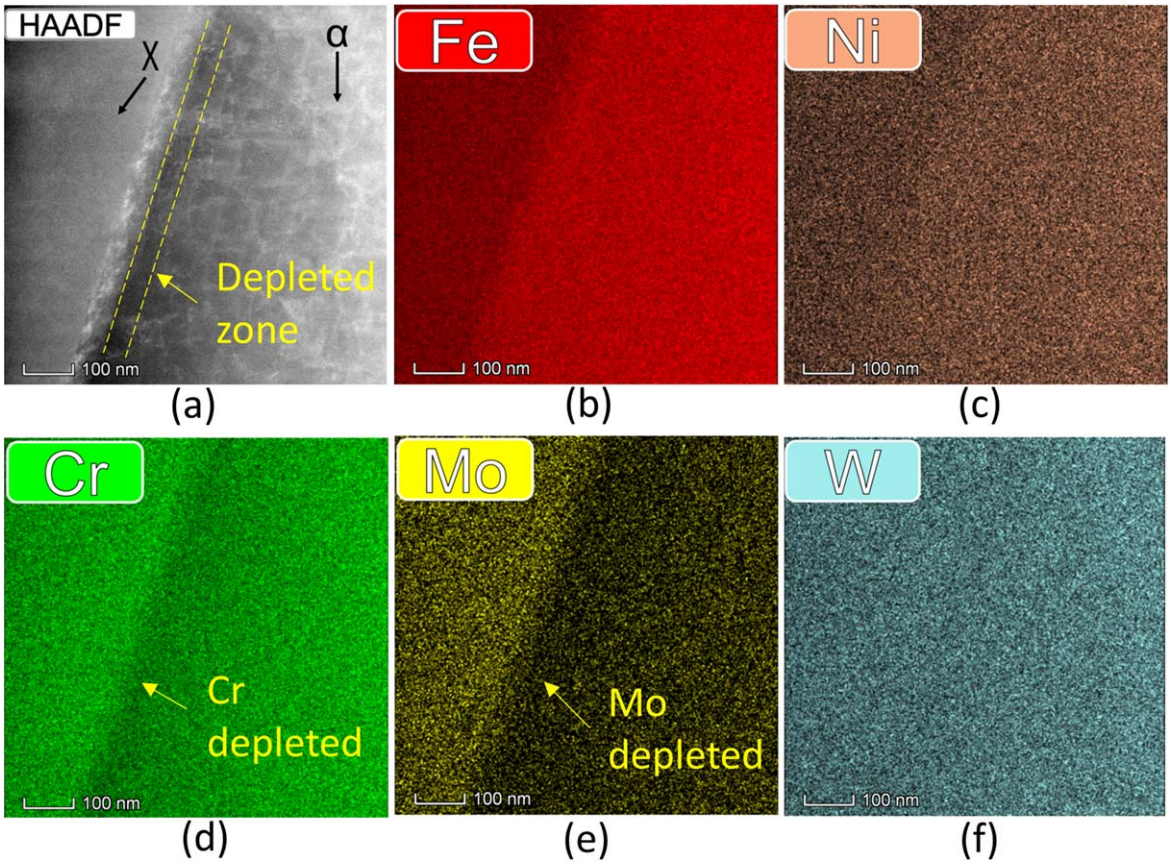

Figure 8. STEM images and elemental maps from EDS maps of χ-phase and α, as indicated. (a) HAADF image and (b) Fe, (c) Ni, (d) Cr, (e) Mo, and (f) W maps. TEM specimen extracted from UNS S39274 steel treated T2 for t6.

Table VII. Heat treatments showing statistically significant differences (p-value < 0.05) in CPT values depending on the material according to Bonferroni and Tukey tests.

Heat treatment T (°C), t (s)	Materials (UNS)	CPT (°C)	Secondary phases (vol%)
790, 240	S32750	65	No precipitates found by SEM
	S32760	55	0.04%
846, 240	S32750	50	0.3% σ
	S39274	65	0.04% χ
846, 240	S32760	45	0.2% σ, 0.2% χ
	S39274	65	0.04% χ
920, 600	S32750	45	3.1% σ, 0.1% χ
	S39274	55	1.72% χ, 0.3% σ
920, 600	S32760	<40	5.1% σ, 0.3% χ
	S39274	55	1.72% χ, 0.3% σ

same aging times for the three different aging temperatures. Those aging times corresponded to CPT values decreasing to below 40 °C and, for UNS S32750, involved a large difference from the previous CPT value. In contrast, UNS S39274 showed moderate CPT drops, as the CPT slowly decreased with IHT time (Fig. 16). As a result, S39274 had more statistically significant differences (p-value $<$ 0.05) with the other two SDSS as showed in Table VII.

The reason for the gradual decrease in CPT with vol% of precipitates observed for UNS S39274 was attributed to the preferential formation of χ-phase instead of σ-phase. The CPT was lower, 10 °C–20 °C depending on the IHT, when σ was the main phase present as seen in Table VII. Because σ-phase is richer in Cr, its precipitation leads to the lowest Cr content in the affected zone adjacent to the precipitates.[29] Consequently, σ-phase has been considered, a priori, the most deleterious IMC in (S)DSS.[29,41] Nevertheless, the presence of χ-phase also affected CPT values apparently to a similar degree than σ-phase when compared at the same volume fraction, which at the same aging temperature implies comparing different IHT times (e.g., Fig. 14 vs Fig. 16).

In all cases, the statistically significant differences in CPT involved only a small total amount of deleterious phases. Indeed, in most situations, the total volume of IMCs was less than 1 vol%, which was lower than the 2–6 vol% localized corrosion threshold reported by Mathiesen et al.[68] and Deng et al.[60]

If instead, the critical volume fraction of deleterious phases is arbitrarily defined according to the conditions at which CPT drops

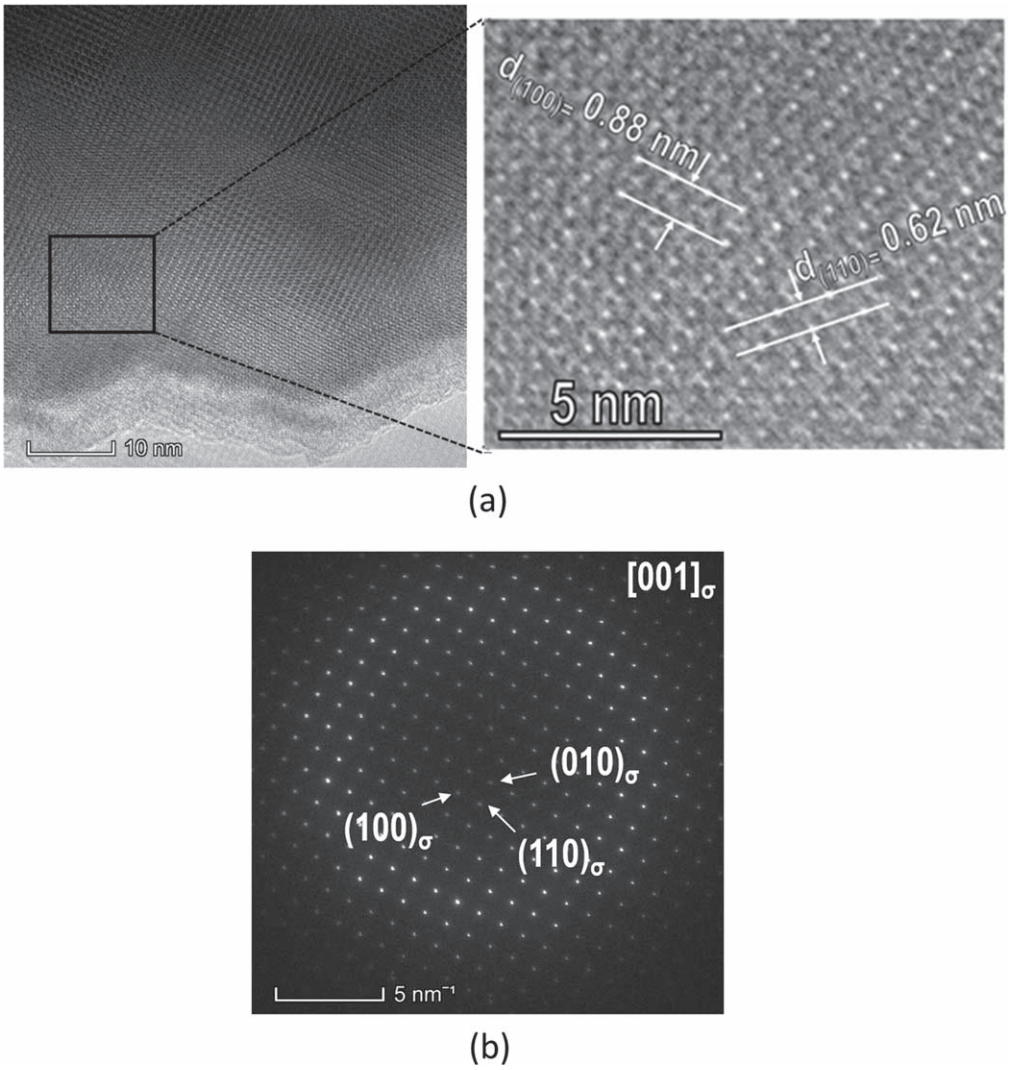

Figure 9. TEM analysis of σ-phase precipitate formed in UNS S32750 steel treated T2 for t4. (a) HR-TEM image and (b) indexed SAD pattern of the σ-phase parallel to the [001] zone axis.

below 40 °C, the quantities of σ- and χ-phase were higher. The volume fraction of tertiary phases that led to a CPT $\leqslant$ 40 °C are gathered in Table VIII for a simpler visualization. The three alloys followed the same trend, i.e., the higher the IHT temperature, the greater the density of intermetallic phases needed to lower the CPT below 40 °C. Furthermore, the same quantity of tertiary phases affected the CPT differently depending on the IHT temperature. For instance, in Fig. 14 there are two different IHT (790 °C, 600 s and 920 °C, 240 s) for UNS S32750 that had completely different CPT values (<40 °C and 70 °C, respectively) although they both contained a similar volume fraction of tertiary phases, i.e., 0.2% σ, 0.1% χ.

Table VIII. Volume fraction of deleterious phases and IHT time at which CPT was below 40 °C for each IHT temperature (values taken from Figs. 14 to 16).

	Heat treatment		
Material (UNS)	T (°C)	t (s)	Critical vol% of deleterious phases
S32750	790	600	0.2% σ, 0.1% χ
	846	600	3.8% σ, 0.3% χ
	920	1200	9.3% σ, 0.1% χ
S32760	790	600	0.9% σ, 0.4% χ
	846	600	2.7% σ, 0.2% χ
	920	600	5.1% σ, 0.3% χ
S39274	790	1200	0.23% σ, 0.21% χ
	846	600	1.4% χ, 0.3% σ
	920	>1200[a)]	>(4.13% χ, 0.8% σ)[a)]

a) CPT was over 40 °C for all IHT times.

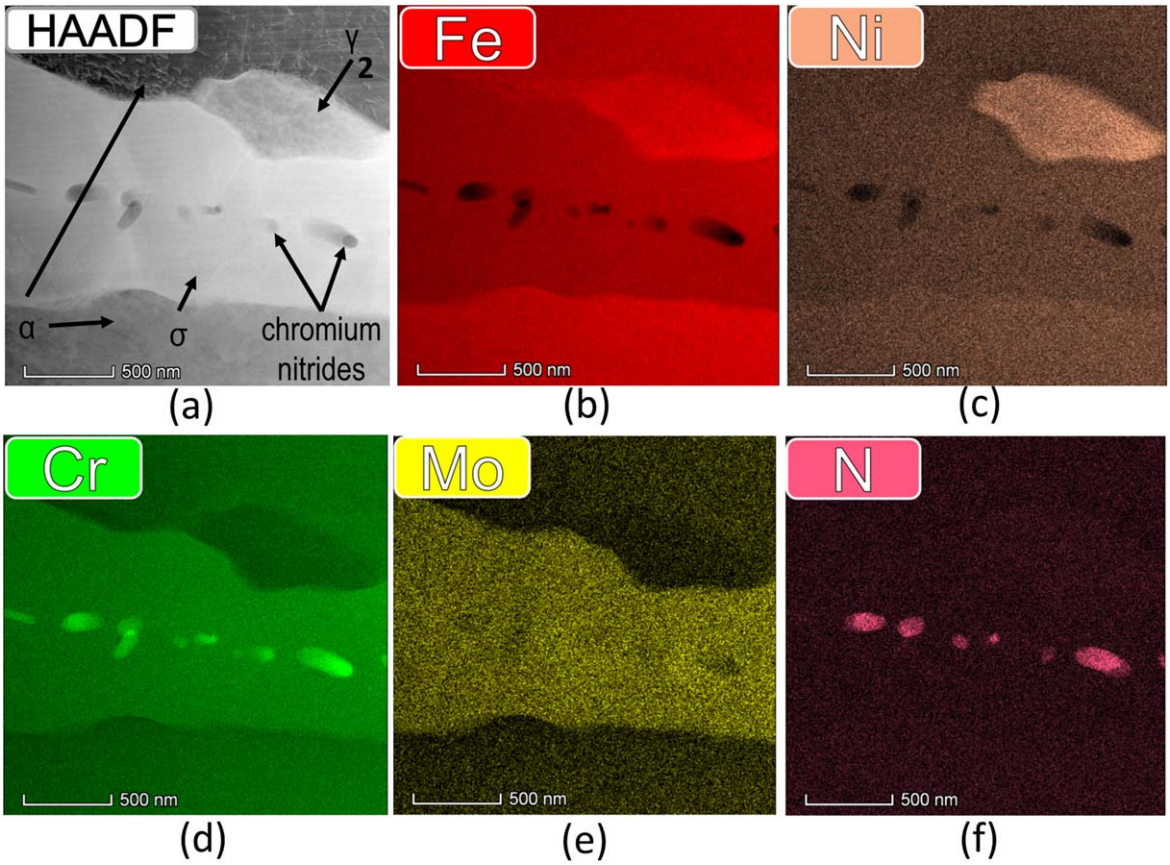

Figure 10. STEM images and elemental maps from EDS spectrum images of σ-phase, chromium nitrides, γ and α, as indicated. (a) HAADF image and (b) Fe, (c) Ni, (d) Cr, (e) Mo, and (f) N maps. TEM specimen extracted from UNS S32750 steel treated T2 for t4.

Nilsson et al.[49] reported similar observations, where different IHTs with the same volume fraction of σ-phase had different CPT values. In their work, the authors suggested that the reduction in localized corrosion resistance is not exclusively related to σ-phase, but the explanation might be related to the other intermetallic phases that were present. Other authors[94] suggested that the depleted zones are richer in Cr and Mo at higher IHT temperatures as the diffusion kinetics increases with temperature. Consequently, comparisons between IHT must be performed within the same temperature and, thus, reporting a unique critical volume fraction of tertiary phases per material is not possible. Instead, each material presented three critical volume fractions, one per IHT temperature, which are summarized in Table VIII. In Table VIII, it was assumed a CPT $\leqslant$ 40 °C to define the critical volume fraction.

Taking the IHT time as the critical parameter, Table VIII shows that UNS S32750 and S32760 shared the shortest critical IHT time at 790 °C. At 846 °C, all three materials attained the same critical IHT time. And finally, at 920 °C, UNS S32760 had the lowest critical IHT time whereas the CPT of S39274 did not drop below 40 °C even at the longest IHT time. Taking into consideration these critical IHT times, it was concluded that the localized corrosion resistance of UNS S39274 was the least affected by IHT; whereas S32760 was the most influenced by it.

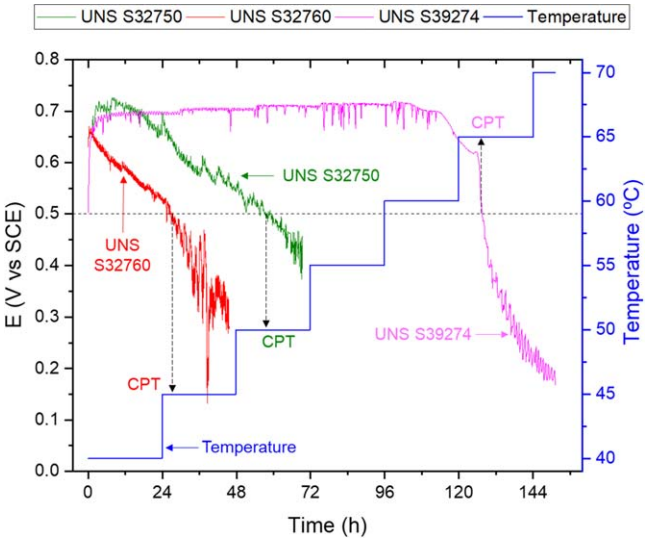

Figure 11. OCP in 6 wt%. $FeCl_3$ as a function of aging time and temperature for the three materials isothermally aged at 846 °C for 240 s, as indicated.

Implications.—The results of this work proved, by different types of analyses, that 2.1 wt% W drastically reduced the kinetics of σ-phase precipitation in UNS S39274, which also suffered the least deterioration of corrosion resistance by IHT. In contrast, UNS S32760 was the most impacted regarding both total precipitates and the corresponding corrosion resistance. Unlike UNS S32750,

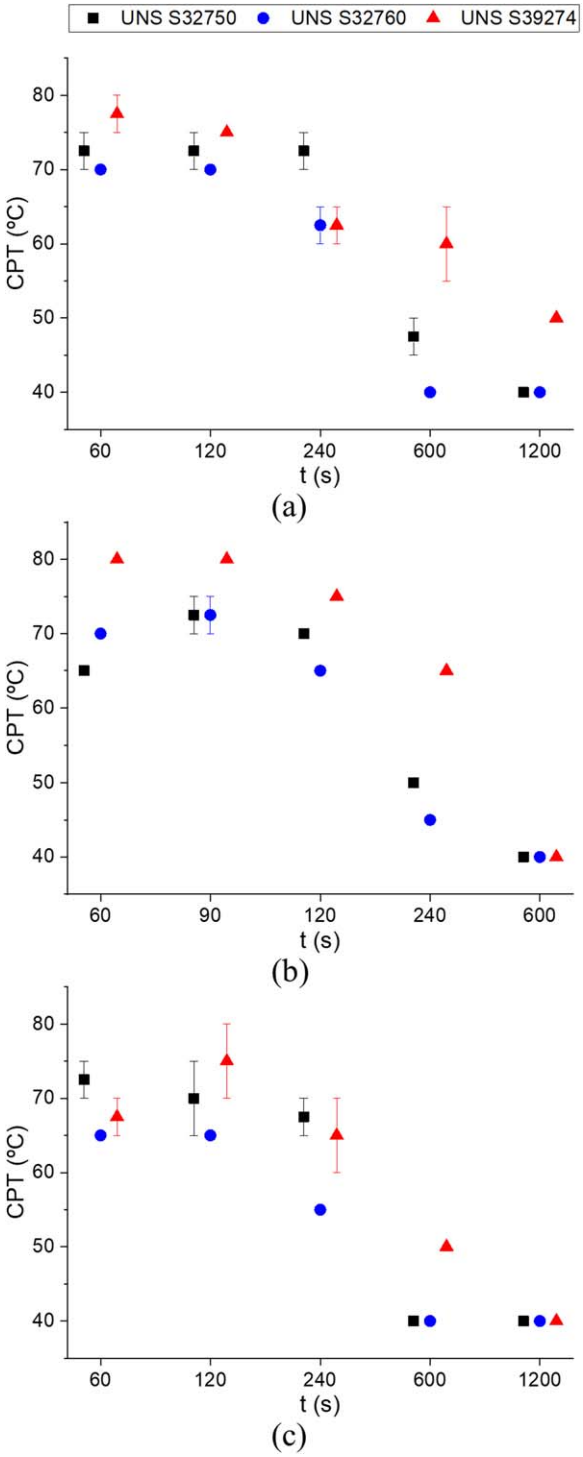

Figure 12. CPT values obtained in all specimens isothermally aged at (a) 920 °C, (b) 846 °C and (c) 790 °C. Error bars represent maximum and minimum values.

both S32760 and S39274 contain different quantities of W, suggesting the existence of an optimal W concentration.

Despite the exhaustive characterization performed herein, there are still some concerns that need to be addressed to quantify the role of W in solid solution and of each of the deleterious phases on the localized corrosion resistance of SDSS. The mechanisms by which W in solid solution influences localized corrosion resistance are yet to be demonstrated. Likewise, the reasons for the apparent optimal W range where the precipitation of σ-phase is kinetically retarded are unclear and contradict modeling work by, e.g., Wessman et al.[40,64] Additionally, although UNS S39274 appears to be within the optimal W concentration, the range within which W is beneficial cannot be inferred from this work.

The precipitation of both σ- and χ-phase led to a sharp decrease in CPT even in concentrations well below the 2–6 vol% threshold suggested by Mathiesen et al.[68] and observed by Deng et al.[60] It cannot be demonstrated conclusively from the results presented herein which phase, σ or χ, is more detrimental regarding corrosion resistance. Moreover, at a similar volume fraction of the same deleterious phase, the aging temperature had also an apparent effect as discussed above. A more detailed TEM, EDS and Auger spectroscopy investigation could shed light on possible compositional gradients at the precipitate/matrix interface as well as their influence on the local stability of the passive films, which could explain the observed corrosion behavior.

Despite these shortcomings, a comparison of UNS S32750 (W-free) and S39274 (high-W) indicated that similar reductions in CPT were measured in samples that had a similar volume fraction of precipitates, where σ-phase was predominant in UNS S32750 and χ-phase in S39274. The main advantage of the high-W SDSS appears to be the sharply slower precipitation kinetics of deleterious phases.

Although all SDSS had similar CPT in the SA condition, the slower precipitation kinetics of deleterious phases in UNS S39274 could be advantageous when welding SDSS components. In this regard, SDSS welding procedures require very low interpass temperatures—often below 150 °C[65]—to prevent the precipitation of deleterious phases. The low interpass temperature extends welding time and increases costs. Given the lower propensity to form deleterious phases of UNS S39274, welding procedures could be optimized by allowing higher interpass temperatures, which could, in turn, lead to economic benefits over other SDSS families. More research is, nonetheless, necessary to validate this hypothesis as the microstructure evolution during welding is more complex than that attained by IHT, and also contradicts the computational thermodynamics modeling work by Wessman et al.[64]

Conclusions

In this work, the effect of W on the precipitation kinetics of deleterious phases of three commercial SDSS was investigated. Additionally, the pitting corrosion resistance was quantified as a function of microstructure evolution after IHT. The following conclusions were drawn based on the evidenced provided above:

- A 2.1 wt% W addition to SDSS retarded σ-phase precipitation and promoted the nucleation of χ-phase. On the other hand, little χ-phase formation was observed in the alloy containing 0.6 wt%. W, which showed the fastest σ-phase precipitation.
- Despite the precipitation of χ-phase, the alloy containing 2.1 wt% W had the lowest total amount of intermetallic phases, whereas UNS S32760 (0.6 wt% W) contained the largest volume fraction of precipitates in almost all IHT conditions.
- CPT values dropped according to the concentration of deleterious phases within the same IHT temperature, indicating a strong correlation between corrosion resistance and tertiary phase precipitation kinetics.
- Both χ- and σ-phase lowered CPT, but the reduction appeared more drastic when σ-phase was the main precipitated phase (UNS S32750 and S32760), rather than χ-phase (10 °C–20 °C difference depending on the IHT).
- Results of the statistical analysis indicated that the decrease in CPT was significant when the concentration of deleterious phases was less than 1.0 vol%.

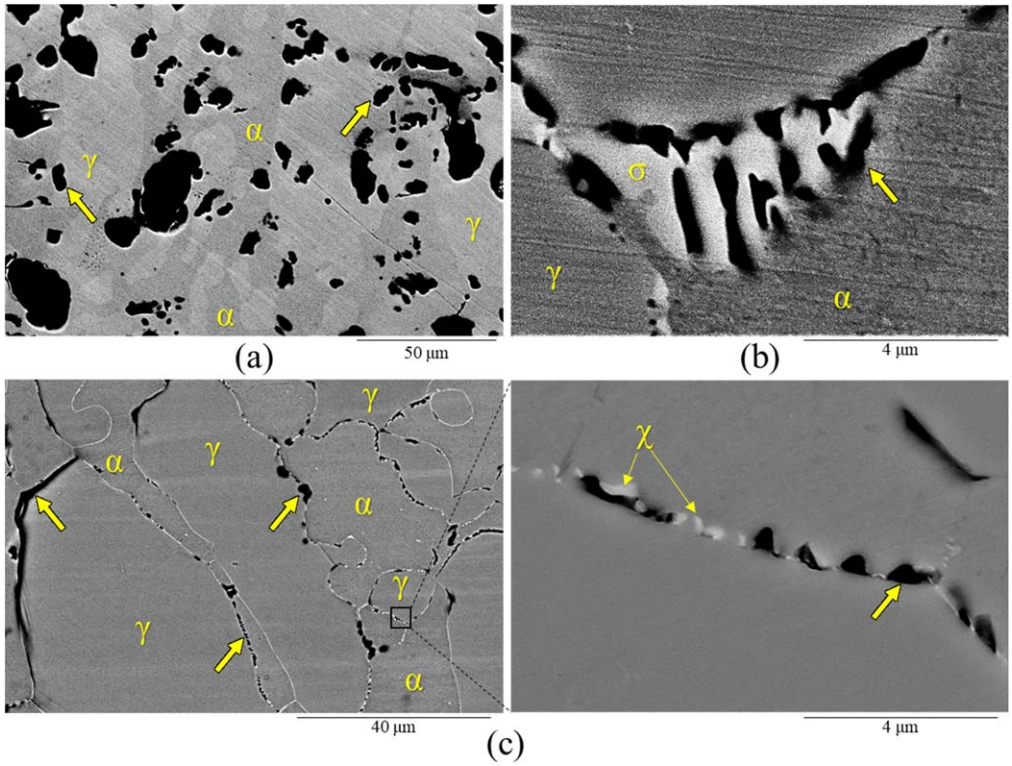

Figure 13. SEM pictures after CPT tests of samples (a) SA UNS 32750 and (b) 790 °C for 1200 s IHT UNS S32750, and (c) UNS S39274 heat treated at 790 °C for 1200 s. Arrows point at the location of some localized attacks.

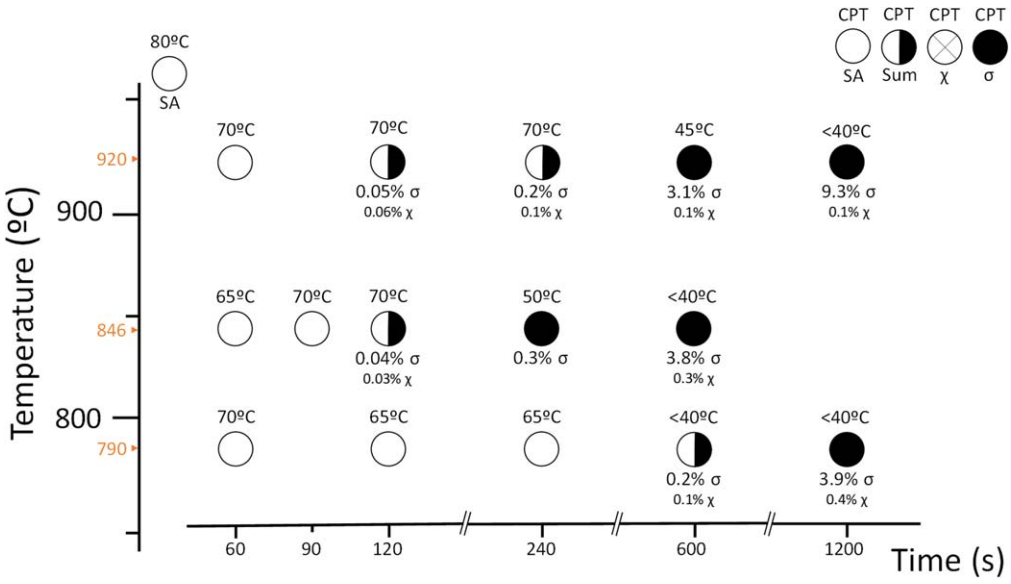

Figure 14. TTTC-diagram for UNS S32750 including vol% of tertiary phases and corresponding CPT values.

- The higher the IHT temperature, the higher the volume fraction of intermetallic phases needed to produce a decrease in CPT below 40 °C. Therefore, each material presented three critical volume fractions of deleterious phases, i.e., one per IHT temperature.
- Considering the IHT time as a critical parameter; UNS S39274 was the material affected the least by IHT, whereas S32760 was influenced the most.
- Results suggested the existence of an optimal W concentration range. Outside this range, W may become detrimental regarding corrosion resistance and precipitation kinetics. Although the optimal minimum and maximum W concentration cannot be inferred from the present study, the results indicated that 2.1 wt% W was inside the range, while 0.6 wt% W might have been outside of it.

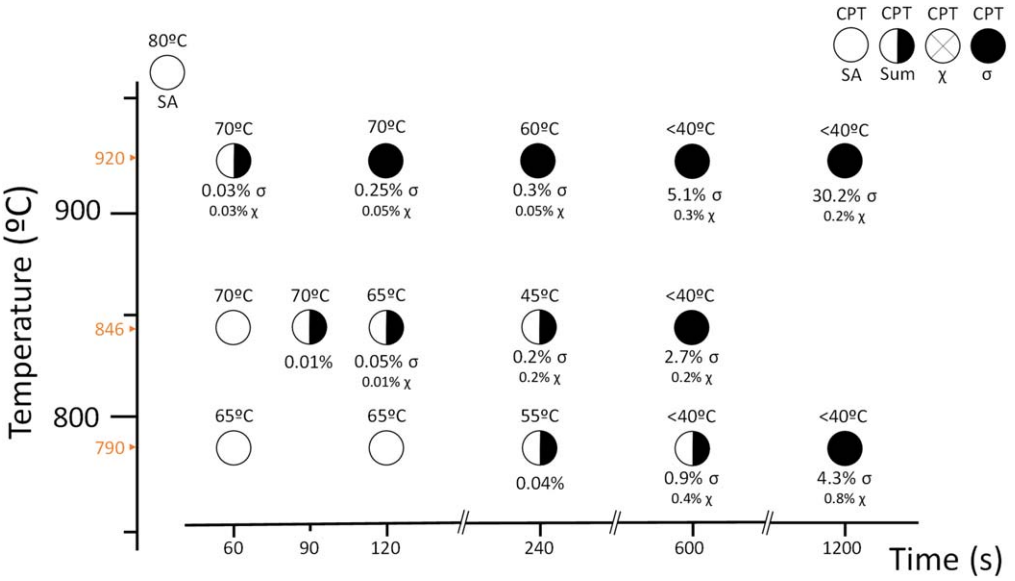

Figure 15. TTTC-diagram for UNS S32760 including vol% of tertiary phases and corresponding CPT values.

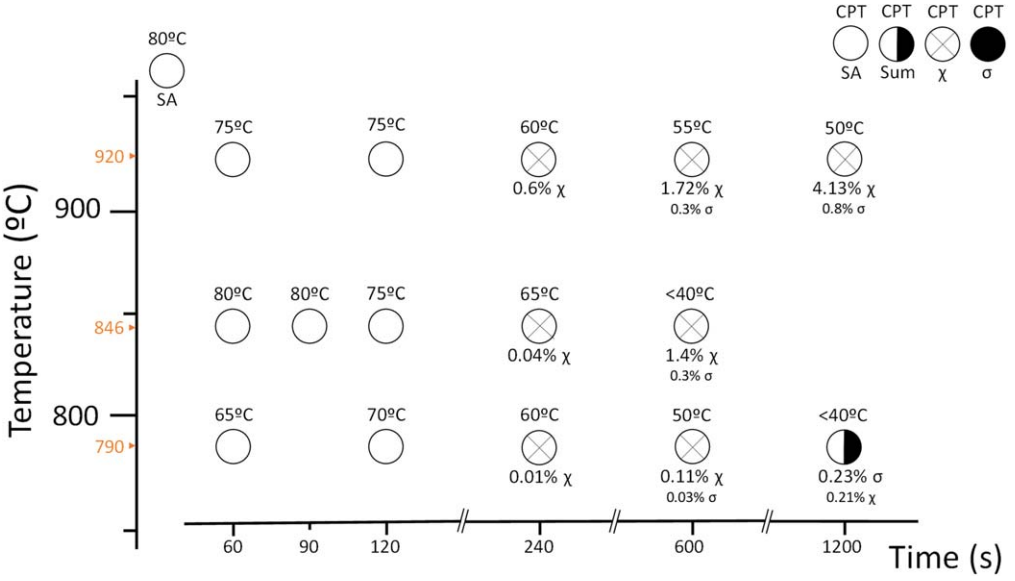

Figure 16. TTTC-diagram for UNS S39274 including vol% of tertiary phases and corresponding CPT values.

Acknowledgments

The authors thank professor Ida Westermann (NTNU), Di Wan (NTNU), Atle H. Qvale (GE O&G), and Anders Jernberg (GE O&G) for their guidance and the technical discussions. The authors also acknowledge Sumitomo Co. and Sandvik AS, who provided the various materials. This work was sponsored in part by General Electric, Co. (Oil and Gas, Norway) and NTNU and conducted at NTNU's Department of Mechanical and Industrial Engineering with the support of master students Hege Østvold, Mia Bernås, and Christian Lauritsen. Lastly, the authors acknowledge the support of the John de Laeter Centre at Curtin University during EBSD and TEM studies.

ORCID

Cristian Torres https://orcid.org/0000-0003-3793-6542
María Sofía Hazarabedian https://orcid.org/0000-0002-8220-3922
Zakaria Quadir https://orcid.org/0000-0003-1626-3748
Roy Johnsen https://orcid.org/0000-0002-5449-7396
Mariano Iannuzzi https://orcid.org/0000-0001-9202-3696

References

1. A. J. Sedriks, *Corrosion*, **42**, 376 (1986).
2. C. O. A. Olsson and D. Landolt, *Electrochim. Acta,*, **48**, 1093 (2003).
3. R. C. Newman, *Corros.*, **57**, 1030 (2001).
4. J. O. Nilsson, *Mater. Sci. Technol.*, **8**, 685 (1992).
5. V. K. Lorenz and G. Médawar, *Thyssenforschung*, **1**, 97 (1969).
6. J. E. Truman, *Proceedings UK Corrosion'87*, Brighton, UK, 111 (1987).
7. R. F. A. Jargelius-Pettersson, *Corros.*, **54**, 162 (1998).
8. E. Alfonsson and R. Qvarfort, *Mater. Sci. Forum*, **111–112**, 483 (1992).
9. J. H. Cleland, *Eng. Fail. Anal.*, **3**, 65 (1996).
10. P. Kangas and G. C. Chai, *Adv. Mater. Res.*, **794**, 645 (2013).
11. J. Charles, "Duplex stainless steels "91." *Proceedings. Les Éditions de Physique Les Ulis*, Beaune, Bourgogne, France, p. 151 (1991).
12. International Organization for Standardization, Switzerland, "ISO 21457:2010." *Petroleum, petrochemical and natural gas industries - Materials selection and corrosion control for oil and gas production systems* (2010).
13. NORSOK M-001, *Materials Selection*, Standards Norway, Lysaker, Norway (2014).
14. R. Francis, G. Byrne, and G. Warburton, *Corrosion 2011*, Houston, TX(NACE International), 11351 (2011).
15. J. Oredsson and S. Bernhardsson, *Mater. Perform.*, **22**35 (1983).
16. R. N. Gunn, *Duplex Stainless Steels: Microstructure, Properties and Applications* (Woodhead Publishing, Cambridge, U.K) (1997).

17. M. Sofia Hazarabedian, A. Viereckl, Z. Quadir, G. Leadbeater, V. Golovanevskiy, S. Erdal, P. Georgeson, and M. Iannuzzi, *Corros.*, **75**, 824 (2019).
18. L. F. Garfias-Mesias and J. M. Sykes, *Corros.*, **54**, 40 (1998).
19. E. B. Haugan, M. Næss, C. Torres Rodriguez, R. Johnsen, and M. Iannuzzi, *Corros.*, **73**, 53 (2017).
20. M. K. Ahn, H. S. Kwon, and H. M. Lee, *Corros. Sci.*, **40**, 307 (1998).
21. J. S. Kim, P. J. Xiang, and K. Y. Kim, *Corros.*, **61**, 174 (2005).
22. H. Habazaki, A. Kawashima, K. Asami, and K. Hashimoto, *Corros. Sci.*, **33**, 225 (1992).
23. C. Jia and W. Jiann Kuo, *Corros. Sci.*, **30**, 53 (1990).
24. A. K. Mishra and D. W. Shoesmith, *Corros.*, **70**, 721 (2014).
25. K. Lutton Cwalina, C. R. Demarest, A. Y. Gerard, and J. R. Scully, *Curr. Opin. Solid State Mater. Sci.*, **23**, 129 (2019).
26. N. Bui, A. Irhzo, F. Dabosi, and Y. Limouzin-Maire, *Corros.*, **39**, 491 (1983).
27. N. D. Tomashov, G. P. Chernova, and O. N. Marcova, *Corros.*, **20**, 166t (1964).
28. A. Belfrouh, C. Masson, D. Vouagner, A. M. de Becdelievre, N. S. Prakash, and J. P. Audouard, *Corros. Sci.*, **38**, 1639 (1996).
29. C.-J. Park, M.-K. Ahn, and H.-S. Kwon, *Materials Science and Engineering: A*, **418**, 211 (2006).
30. E.-A. Cho, C.-K. Kim, J.-S. Kim, and H.-S. Kwon, *Electrochim. Acta*, **45**, 1933 (2000).
31. K. Ogawa, H. Okamoto, M. Ueda, M. Igarashi, T. Mori, and T. Kobayashi, *Weld. Int.*, **10**, 466 (1996).
32. K. Ogawa, H. Okamoto, M. Igarashi, M. Ueda, T. Mori, and T. Kobayashi, *Weld. Int.*, **11**, 14 (1997).
33. Y. S. Ahn and J. P. Kang, *Mater. Sci. Technol.*, **16**, 382 (2000).
34. K. Ogawa and T. Osuki, *ISIJ Int.*, **59**, 129 (2019).
35. K. Ogawa and T. Osuki, *ISIJ Int.*, **59**, 122 (2019).
36. J. O. Nilsson, T. Huhtala, P. Jonsson, L. Karlsson, and A. Wilson, *Metall. Mater. Trans. A*, **27**, 2196 (1996).
37. K. Y. Kim, P. Q. Zhang, T. H. Ha, and Y. H. Lee, *Corros.*, **54**, 910 (1998).
38. J. S. Kim and H. S. Kwon, *Corros.*, **55**, 512 (1999).
39. H. J. Park and H. W. Lee, *Int J Electrochem Sc*, **9**, 6687 (2014).
40. S. Wessman and R. Pettersson, *Steel Res. Int.*, **86**, 1339 (2015).
41. S. Hertzman, T. Huhtala, L. Karlsson, J. O. Nilsson, M. Nilsson, R. Jargelius-Pettersson, and A. Wilson, *Mater. Sci. Technol.*, **13**, 604 (1997).
42. Y. H. Lee, K. T. Kim, Y. D. Lee, and K. Y. Kim, *Mater. Sci. Technol.*, **14**, 757 (1998).
43. A. R. Akisanya, U. Obi, and N. C. Renton, *Materials Science and Engineering: A*, **535**, 281 (2012).
44. J. S. Kim, T. H. Ha, and K. Y. Kim, *Corros.*, **57**, 452 (2001).
45. S.-H. Jeon, S.-T. Kim, I.-S. Lee, J.-S. Kim, K.-T. Kim, and Y.-S. Park, *J. Alloys Compd.*, **544**, 166 (2012).
46. R. Goetz, J. Laurent, and D. Landolt, *Corros. Sci.*, **25**, 1115 (1985).
47. T.-H. Lee and S.-J. Kim, *Scr. Mater.,*, **39**, 951 (1998).
48. N. Llorca-Isern, H. López-Luque, I. López-Jiménez, and M. V. Biezma, *Mater. Charact.,*, **112**, 20 (2016).
49. J. O. Nilsson and A. Wilson, *Mater. Sci. Technol.*, **9**, 545 (1993).
50. C. Örnek and D. L. Engelberg, *J. Mater. Sci.,*, **51**, 1931 (2016).
51. R. Magnabosco, *Mater. Res.*, **12**, 321 (2009).
52. R. Magnabosco, L. da Costa Morais, and D. C. dos Santos, *Calphad*, **64**, 126 (2019).
53. R. Magnabosco and N. Alonso-Falleiros, *Corros.*, **61**, 130 (2005).
54. D. Caluscio dos Santos, R. Magnabosco, and C. de Moura-Neto, *Corros.*, **69**, 900 (2013).
55. D. Y. Kobayashi and S. Wolynec, *Mater. Res.*, **2**, 239 (1999).
56. D. M. E. Villanueva, F. C. P. Junior, R. L. Plaut, and A. F. Padilha, *Mater. Sci. Technol.*, **22**, 1098 (2006).
57. I. Calliari, M. Pellizzari, and E. Ramous, *Mater. Sci. Technol.*, **27**, 928 (2011).
58. N. Llorca-Isern, I. López-Jiménez, H. López-Luque, M. V. Biezma, and A. Roca, *Mater. Sci. Forum*, **879**, 2537 (2016).
59. C.-C. Hsieh and W. Wu, *ISRN Metall.*, **2012**, 1 (2012).
60. B. Deng, Z. Wang, Y. Jiang, H. Wang, J. Gao, and J. Li, *Electrochim. Acta*, **54**, 2790 (2009).
61. N. Pettersson, R. F. A. Pettersson, and S. Wessman, *Metall. Mater. Trans. A*, **46**, 1062 (2015).
62. H. Kokawa, E. Tsory, and T. H. North, *ISIJ Int.*, **35**, 1277 (1995).
63. J. Liao, *ISIJ Int.*, **41**, 460 (2001).
64. S. Wessman, L. Karlsson, R. Pettersson, and A. Östberg, *Weld. World*, **56**, 79 (2013).
65. International Molybdenum Association, London, UK, *Practical guidelines for the fabrication of duplex stainless steels* (2009).
66. A. P. Miodownik and N. Saunders, *Mater. Sci. Technol.*, **18**, 861 (2002).
67. J. O. Nilsson, P. Kangas, A. Wilson, and T. Karlsson, *Metall. Mater. Trans. A*, **31**, 35 (2000).
68. T. Mathiesen and C. Jensen, *CORROSION 2013* (NACE International, Orlando, Florida) (2013).
69. Statoil ASA, "MAT-2010080." *Technical Note - Metallographic Etching of Duplex Stainless Steels* (2010).
70. M. M. Nowell, R. A. Witt, and B. W. True, *Microsc. Today*, **13**, 44 (2005).
71. D. Wan and A. Barnoush, *Materials Science and Engineering: A*, **744**, 335 (2019).
72. D. Wang, X. Lu, D. Wan, Z. Li, and A. Barnoush, *Scr. Mater.*, **173**, 56 (2019).
73. S. He, M. Saunders, K. Chen, H. Gao, A. Suvorova, W. D. A. Rickard, Z. Quadir, C. Q. Cui, and S. P. Jiang, *J. Electrochem. Soc.*, **165**, F417 (2018).
74. D. Tomus and H. P. Ng, *Micron*, **44**, 115 (2013).
75. E. M. L. E. M. Jackson, P. E. D. Visser, and L. A. Cornish, *Mater. Charact.*, **31**, 185 (1993).
76. M. Iannuzzi, C. Mendez, L. Avila-Gray, G. Maio, and H. Rincón, *Corros.*, **66**, 045003-1 (2010).
77. T. Mathiesen, T. S. Nielsen, T. Haugen, B. Espelid, P. Hummelgaard, and K. Vilpponen, *NT Technical Report - Improved Method for ASTM G48 Corrosion Testing of Welds*, Nordic Innovation Centre, Oslo, Norway (2004).
78. T. W. MacFarland, *Two-Way Analysis of Variance. Statistical Tests and Graphics Using R* (Springer, New York) (2012).
79. H. Abdi and L. J. Williams, *Encyclopedia of Research Design*, ed. N. J. Salkind (SAGE Publications, Thousand Oaks, CA) (2010).
80. J. P. Shaffer, *Annual Review of Psychology*, **46**, 561 (1995).
81. T. V. Perneger, *Brit. Med. J.*, **316**, 1236 (1998).
82. D. C. Montgomery, *Design and Analysis of Experiments* (John Wiley & Sons, Inc, Hoboken, NJ) (2009).
83. D. M. Escriba, E. Materna-Morris, R. L. Plaut, and A. F. Padilha, *Mater. Charact.*, **60**, 1214 (2009).
84. J. M. Pardal, S. S. M. Tavares, M. D. P. C. Fonseca, J. A. D. Souza, L. M. Vieira, and H. F. G. D. Abreu, *Mater. Res.*, **13**, 401 (2010).
85. J. M. Pardal, S. S. M. Tavares, M. P. Cindra Fonseca, M. R. da Silva, and M. L. R. Ferreira, *Mater. Sci. Technol.*, **28**, 295 (2012).
86. K. W. Andrews, *Nat.*, **164**, 1015 (1949).
87. G. Bergman and D. P. Shoemaker, *Acta Crystallogr.*, **7**, 857 (1954).
88. J. O. Nilsson, L. Karlsson, and J. O. Andersson, *Mater. Sci. Technol.*, **11**, 276 (1995).
89. A. Irhzo, Y. Segui, N. Bui, and F. Dabosi, *Corros. Sci.*, **26**, 769 (1986).
90. H. M. Lee, S. M. Allen, and M. Grujicic, *Metall. Trans. A*, **22**, 2869 (1991).
91. H. Nitta, T. Yamamoto, R. Kanno, K. Takasawa, T. Iida, Y. Yamazaki, S. Ogu, and Y. Iijima, *Acta Mater.*, **50**, 4117 (2002).
92. S. Takemoto, H. Nitta, Y. Iijima, and Y. Yamazaki, *Philos. Mag.*, **87**, 1619 (2007).
93. P. J. Alberry and C. W. Haworth, *Met. Sci.*, **8**, 407 (1974).
94. E. Angelini, B. De Benedetti, and F. Rosalbino, *Corros. Sci.*, **46**, 1351 (2004).